Photoionization study using few attosecond pulses and coincidence imaging techniques

A thesis presented for the degree of
Master of Science

Lisa Rämisch
Supervised by Mathieu Gisselbrecht and Yu-Chen Cheng
8 months half-time

Acronyms

ANACONDA	Analysis of coincidence data
APT	Attosecond Pulse Train
CEP	Carrier-to-envelope phase
CIEL	Coincidences entre ions et electrons localisés
DLD	Delay-line-detector
EWP	Electron-wave-packet
GUI	Graphical user interfac
HHG	High harmonic generation
IR	Infrared
MCP	Mutltichannel plate
SAP	Single attosecond pulse
SFA	Strong field approximation
TDSE	Time-dependent Schrödinger equation
TOF	Time-of-flight
XUV	Extreme ultraviolet
3D	Three-dimensional

Abstract

Photoionization is one of the most fundamental photoreactions that leads to the ejection of an electron and the formation of an ion. With the help of modern 3D momentum imaging spectrometers, the interplay between the time and frequency domain upon ionization is studied.

In this work, single photoionization of helium is investigated in the few-cycle pulse regime of the driving infrared laser pulses with ultrashort attosecond pulses in a dressing infrared field. By varying the carrier-to-envelope phase of the infrared field to modify the spectro-temporal structure of the attosecond pulses, we analyze how the infrared field impacts the measured angularly-resolved photoelectron energy distribution. To this end, a newly built coincidence 3D momentum spectrometer was used. A thorough understanding of the experiment is achieved by using simulations within the strong field approximation. This analysis allows us to separate our observation into two scenarios, one at two attosecond pulses when the carrier-to-envelope phase is $\pi/2$ and the second one at three attosecond pulses when the carrier-to-envelope phase is 0 or π. When the dressing infrared field is added, the photoelectron spectrum changes in comparison to photoionization with attosecond pulses only. While two attosecond pulses in the dressing infrared field modify the photoelectron spectrum in a continuous way, we observe sidebands appearing in the spectrum generated by three pulses in the dressing infrared field.

Finally, the resolution of the spectrometer is studied before and after an upgrade of the spectrometer was performed in the context of this work. This study allows us to understand the limiting factors of the energy resolution. In particular, it shows that the resolution is essentially limited by the source volume of the emitted particles, while the magnetic field does not limit the resolution as it was expected.

Contents

Chapter 1

Introduction

Since the first experimental measurement of attosecond pulses in 2001 [35], large efforts have been dedicated to study electron dynamics and, in particular, to investigate real time dynamics of one of the most fundamental processes caused by light-matter-interaction, photoionization. While the release of an electron during ionization was long thought to be instantaneous, pump-probe experiments [11, 13, 21]) have revealed that it occurs with a time-delay on the attosecond timescale (10^{-18} s). In addition to the study of time delay in atoms, the quantum coherence in photoionization [5], as well as dissociative photoionization in molecules have been investigated [42]. Recent developments allow us to gain new insights into how photoionization can be controlled and studied [18, 33].

In order to measure the photoelectron dynamics upon ionization, several spectrometers have traditionally been employed in the attosecond research groups in Lund, such as the magnetic-bottle-spectrometer (MBES) [16] and the velocity-map-imaging (VMI) spectrometer [38]. The results obtained with the VMI have shown that the photoelectron time delay depends on the angular emission direction [3]. In the case of the VMI and MBES, however, direct information about the momentum of the emitted particle direction in three dimensional space is lost. Therefore, a new compact momentum imaging spectrometer was built allowing to collect a complete 3D data set with a 4π collection efficiency. An important advantage with the new imaging apparatus is the possibility to collect electrons and ions in coincidence. As the word coincidence suggests, only the electron and its parent ion ought to be collected at the same time in order to relate them to each other. This potentially opens the door for the development of different kinds of experiments on atoms and molecules.

The creation of at most one electron-ion pair per laser shot requires low pulse energy. Additionally, the low event rate leads to very long acquisition times. These technical challenges are solved by a new state-of-the-art laser which provides few-cycle femtosecond pulses with several μJ at a high repetition rate on the order of megahertz (MHz) [39]. The new properties of these pulses change the traditional physics behind the photoionization process which is studied for the first time as part of this thesis within the MHz group in Lund. Together with the experimental results, the photoionization process is simulated with a semiclassical model allowing us to gain information about the

light-matter-interaction itself.

Three dimensional data imply large amount of ionization events to be generated in order to obtain high enough statistics of the studied process. Afterwards, the big data set needs to be processed in order to extract physical information. Large data treatment has been addressed in this thesis through a generalized data analysis program [4]. Thereby, the calibration, representation and filtering of the data has played an important role to for example study which factors limit the resolution of the spectrometer.

1.0.1 Thesis work and Outline

The motivation of this thesis is primarily to improve the coincidence imaging tool developed in Lund. An improvement with regards to the spectrometer is made by redesigning the setup and the energy resolution of the spectrometer is studied. These resolution studies are indispensable in order to know the conditions under which future experiments can be conducted. Hereby, the resolution is studied both before and after the new design of the setup and the factors that limit the resolution are discussed. Finally, a data analysis tool is programmed to easily convert data from the imaging spectrometer. It is used to look at data from the first photoionization experiment performed in the group. The data are analyzed, an analytical model is introduced and the results are interpreted using an analogy to a slit experiment. This thesis work includes both experimental and theoretical investigations and is presented in three main parts.

In *chapter 2*, the basic concepts of light-matter-interaction are introduced. The process of generating attosecond pulses is presented which is important to understand the experiment discussed in this thesis where attosecond pulses are used to create photoelectrons. Furthermore, for the analysis of the experimental results, it is important to understand how the phase of these attosecond pulses varies. A recently developed model that expresses the different dependencies of the phase is introduced. Moreover, since photoionization is studied with a dressing field that changes the kinetic energy of the electron, the theoretical model, that we use to simulate and interpret the results, is derived.

Chapter 3 has the main objective to explain the experimental methods. In the beginning, the main concept of the experiment is presented as well as the imaging spectrometer used to collect the experimental data. We show the comparative advantage of the spectrometer design in Lund. In the next step, the basic idea behind the data analysis program and the presentation of the data is shown. Finally, the protocol for performing a calibration and resolution experiment is explained and the main steps in order to extract the resolution value.

In *chapter 4*, the results from the photoionization experiment and the resolution study are displayed, explained and interpreted. Thereby, the observations made during the photoionization experiment are split into two distinguishable parts in order to facilitate the analysis.

Since this thesis opens up many doors for future investigations and experiments, a quick outlook for upcoming projects is given in the end of the report.

Chapter 2

Background

One of the studies performed within the frame of this thesis work is based on light-matter-interaction using attosecond pulses. This chapter presents the necessary background to understand how attosecond pulses are generated and how the phase of these pulses can be controlled. Lastly, we present the principle behind photoionization in the presence of an IR dressing field.

In general, an ultrashort pulse is described by its amplitude and its temporal phase [41]. The amplitude varies over the duration of the pulse and is defined by a time-dependent envelope $E_0(t)$. The temporal phase describes how the electric field oscillates below this envelope. At a central wavelength λ, the pulses propagate at an angular frequency $\omega = \frac{2\pi c_0}{\lambda}$, where c_0 is the speed of light in vacuum. The direction of propagation is defined by the wavevector $\mathbf{k}$ and the polarization of the field is considered to be linear. The time-dependent amplitude of the electric field is given by

$$\mathbf{E}(t) = Re\{E_0(t)\,e^{-i\omega t+i\varphi}\}\hat{\mathbf{z}}, \tag{2.1}$$

where $\hat{\mathbf{z}}$ is the polarization direction. The phase offset φ, referred to as carrier-to-envelope-phase (CEP), is discussed later in this chapter, as it is important for this thesis.

2.1 Attosecond Light Source

After the invention of chirped pulse amplification (CPA) [44] in 1985, it was possible to obtain conventional femtosecond laser pulses with high intensity ($\geq 10^{13}$ W/m^2), allowing researchers to study light-matter-interactions in strong fields [2, 27]. From these studies, a variety of light sources have been developed [36, 43]. In the last decades attosecond light sources in the extreme ultraviolet (XUV) regime, either based on attosecond pulse trains (APTs) or single attosecond pulses (SAPs), have enabled the study of electron dynamics in time-resolved experiments [28] .

Attosecond light sources are created by tightly focusing an infrared (IR) laser field into a noble gas jet. At the focus, intensities on the order of $10^{13} - 10^{14}$W/cm^2 are reached [26] where the laser field amplitude is comparable to the electric field of the atom. As a

result of this highly nonlinear interaction, temporally coherent XUV light bursts, phase-locked to the IR field, are produced with a duration of a few hundreds of 10^{-18} s. These attosecond pulses are generated by a process called high-harmonic-generation (HHG) which is presented in more detail in the following [31].

To explain the spectro-temporal properties of HHG, a classical three-step-model was introduced in 1993 [8]. Through the interaction with a strong laser field, the Coulomb potential of the atom can be distorted. As a consequence, the valence electron can tunnel out into the continuum through the barrier (step 1) at time t_i. Once in the continuum, the electron motion is driven by the laser electric field $E(t) = E_0 \sin(\omega_0 t)$ which oscillates so that the electron is directed back to the parent ion (step 2) at the return time t_r. Lastly, the electron may recombine with the atom and the excess energy acquired in the laser field is emitted as XUV attosecond pulses (step 3).

From the three-step-model, the motion of the electron in the laser field can be described by a classical derivation in atomic units

$$x(t) = \frac{E_0}{\omega^2} (\sin(\omega t) - \sin(\omega t_i) - \omega(t - t_i) \cos(\omega t_i)). \tag{2.2}$$

where E_0 is the maximum amplitude of the electric field. Since the amplitude of the IR field is strong enough, an electron can tunnel out from the atom at more than one moment along the IR field. There is a range of ionization times, t_i, resulting in a range of electron trajectories in the laser field before they recombine at different times t_r.
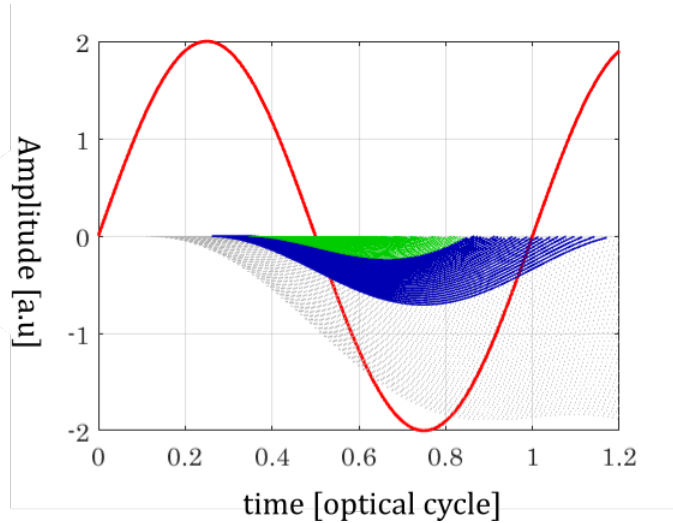

Figure 2.1.1: Illustration of the electron trajectories originating from the HHG process. In red, the IR field used to generate harmonics is drawn. The electrons tunnel out at different ionization times t_i and recombine at different times t_r. Only electrons that recombine are shown in green and blue and correspond to short and long trajectories respectively [47]. The electrons shown by trajectories in gray do not recombine.

Figure 2.1.1 shows the IR laser field amplitude in red over 1.2 cycles and the various electron trajectories emerging from an ionization moment t_i. The electrons that do not

manage to recombine with the parent ion are represented by the trajectories in gray. In blue and green, we plot the so-called long and short trajectories respectively. In this work, only the short trajectories in green are taken into account. Each of these trajectories contributes to the harmonic emission. Since each trajectory corresponds to a different acquired kinetic energy of the electron, the kinetic energies and therefore the frequency components are emitted at different ionization times t_i. The emission encounters a spread of instantaneous frequencies, known as attochirp [20, 45] which can be expressed as a time delay by

$$\tau_{XUV} = \frac{2\gamma}{I}(\Omega - \Omega_p)\omega, \tag{2.3}$$

where I is the intensity at the focus and Ω_p represents the frequency at the ionization threshold I_p of the noble gas. The definition for the term γ in equation 2.3 is given in [17] such that

$$\gamma = \frac{(t_c - t_p)I}{6.4U_p} \tag{2.4}$$

where t_c and t_p are the times corresponding to Ω_c and Ω_p. Ω_c describes the frequency at the cut-off of the spectrum, which is defined at $I_p + 3.2U_p$ [46].

The HHG mechanism is intensity dependent and can occur at every half-cycle of the driving laser field with varying direction. Since the attosecond pulses are temporally co-herent, they interfere in the frequency domain resulting in odd multiples of the central frequency ω (also referred to as odd harmonics). Given that a pulse of very short dura-tion in time domain corresponds to a very broad bandwidth in frequency space, we can deduce that in order to obtain pulses at the order of an attosecond, a large number of odd harmonic frequencies is included in the spectrum.

Given that one attosecond pulse is emitted every half-cycle of the IR laser, π/ω, situated at times equal to $t \to m\pi/\omega$, the number of attosecond pulses can be controlled by varying the duration of the IR pulses. At a wavelength of 800 nm, one IR cycle lasts for roughly 2.6 fs. Consequently, the longer the IR pulse, the more attosecond pulses are emitted resulting in an attosecond-pulse-train (APT). However, at a very short IR pulse of a few femtoseconds, only one half cycle is intense enough to initiate the HHG process and one single attosecond pulse (SAP) is emitted. In this thesis, we work in a regime where the IR pulses include very few cycles of the electric field and therefore only generate a handful of attosecond pulses.

2.2 Few cycle pulse regime

The laser system used to drive the attosecond light source in this thesis is a state-of-the-art high-repetition-rate laser system based on optical parametric chirped pulse amplification (OPCPA) [48], at a repetition rate of 0.2 MHz, with a pulse duration equal to or less than 7 fs. At a central wavelength $\lambda \approx 800$nm, the period of the IR field, calculated by $T = \frac{2\pi c}{\lambda}$, is about 2.6 fs. The laser pulses therefore only cover a few cycles of the IR electric field.

In this few-cycle regime, the difference between the phase and group velocity becomes significant. The complex envelope travels at the so-called group velocity $v_g = \frac{\partial \omega}{\partial \beta}$ where $\beta = \omega \frac{n(\omega)}{c_0}$ where $n(\omega)$ is the refractice index of the gas medium through which the laser field propagates. At the same time, the oscillating electric field underneath the envelope moves a the phase velocity $v_\phi = \frac{\omega}{k}$ where $k = 2\pi/\lambda$ is the wave-vector. Any difference of these two velocities leads to a varying offset of the envelope maximum to the maximum of the underlying field.
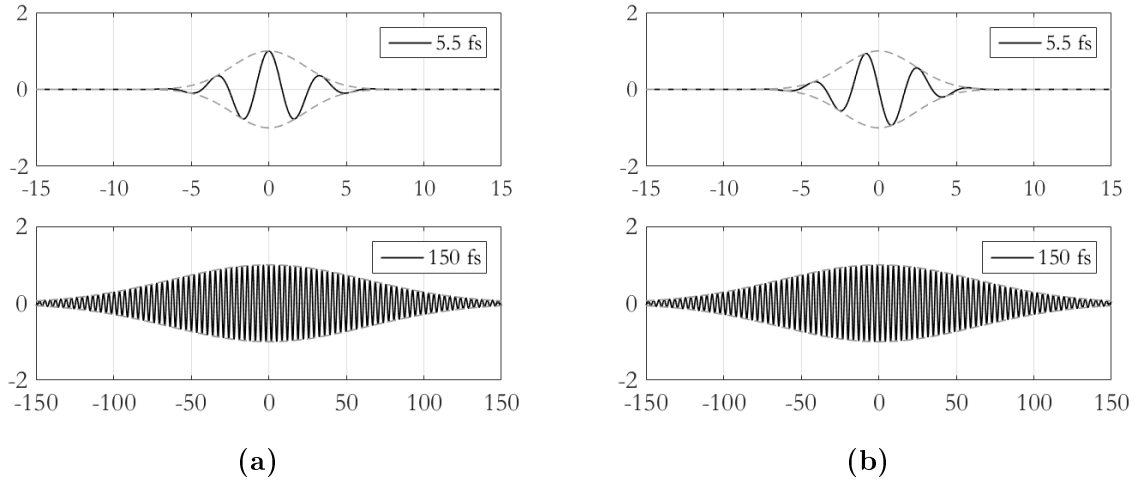

(a)   (b)

Figure 2.2.1: Single ultrashort pulse with a gaussian envelope, a maximum amplitude of 1 and a short (5.5 fs) and long (150 fs) pulse duration at a CEP of (a) 0 and (b) $\pi/2$.

In figure 2.2.1, the electric field for two different pulse durations at two different CEP values is presented. While for a pulse of 5.5 fs a clear change of the electric field can be detected, the change in CEP from figure 2.2.1a to figure 2.2.1b does not produce a noticable difference for a pulse of 150 fs. In order to insure a constant offset between the oscillating field and its envelope, the OPCPA laser system is actively stabilized, also referred to as CEP-stable [18]. The CEP influences the phase of the generated attosecond pulses [17]. An extension of the three-step-model was developed by our group establishing how the APT varies with the CEP and with the number of attosecond pulses in the train. In this model, the phase of the individual attosecond pulses becomes [17]

$$\Phi(\Omega) = z(\Omega) + m\,f(\Omega) + m^2\,s(\Omega). \tag{2.5}$$

Here, m represents the index of an individual attosecond pulse in a train, taking for reference the central pulse given by $m = 0$. The functions z, f and s can be approximated by

$$z(\Omega) \approx \frac{\gamma}{I_{max}} \cdot (\Omega - \Omega_p), \tag{2.6a}$$

$$f(\Omega) = \pi + \frac{\pi\Omega}{\omega} + \varphi\kappa(\Omega), \tag{2.6b}$$

$$s(\Omega) = -\frac{\pi\kappa(\Omega)}{2}, \tag{2.6c}$$

where φ is the CEP of the IR pulse, Ω the XUV frequency, I_{max} the maximum IR intensity, and Ω_p and γ are quantities defined earlier in this chapter. $\kappa(\Omega)$ is expressed as

$$\kappa(\Omega) \approx -\frac{2\pi\gamma}{\omega^2\tau^2 I_{max}}(\Omega - \Omega_p)^2. \tag{2.7}$$

For detailed derivation of the above equations, please refer to [17]. One can notice that $z(\Omega)$ is linearly and $\kappa(\Omega)$ is quadratically proportional to the attochirp. Additionally, $\kappa(\Omega)$ is inversely proportional to the duration of the IR pulses τ and is therefore of importance for attosecond light sources driven by a few-cycle laser as we have it.

For $m = 0$, the phase is influenced by only $z(\Omega)$ while for $m \neq 0$, all three terms contribute to the phase. It can therefore be interpreted as adding a phase contribution to the central attosecond pulse. The second contributing term $f(\Omega)$ is proportional to the CEP φ. The phase difference of π between the consecutive attosecond pulses, expressed in $f(\Omega)$, is an intrinsic property of the HHG process due to a change of the IR field upon tunnel ionization and recombination. Lastly, $s(\Omega)$ affects the separation in time between consecutive attosecond pulses. The field of those pulses in frequency space can be written as follows

$$E_m(\Omega) = e^{iz(\Omega)} \sum_m |A_0(\Omega)| \, (-1)^m \, e^{im\frac{\pi\Omega}{\omega}} \, e^{i\kappa(\Omega)(\phi m - \frac{m^2}{2})} \tag{2.8}$$

where $|A_0(\Omega)|$ is the absolute value of the spectral envelope. In simulations performed within this thesis, the spectral intensity is chosen to be a super-gaussian envelope,

$$A_0(\Omega) = e^{(\frac{\Omega - \Omega_m}{\Omega_w})^4}, \tag{2.9}$$

where Ω_m is the mean value of Ω_c and Ω_p and Ω_w is the difference of the same two frequencies. We choose a super-gaussian envelope because it most closely represents the flat-top plateau of the harmonics.

2.3 Light-Matter-Interaction

In a quantum mechanical treatment, the temporal evolution of an electronic state $|\Psi(t)\rangle$ under the influence of perturbing electromagnetic fields is described by the time-dependent Schrödinger equation (TDSE)

$$\left[\hat{T} + \hat{V}_I(t) + \hat{V}(r)\right] |\Psi(t)\rangle = i\hbar\frac{\partial}{\partial t} |\Psi(t)\rangle \tag{2.10}$$

where $\hat{T}$ stands for the kinetic energy operator, $\hat{V}(r)$ for the Coulomb potential operator and $\hat{V}_I$ for the perturbation by the electromagnetic fields [40]. In the following, atomic units are used, unless stated otherwise. Under the influence of the electromagnetic fields, the system can undergo a transition from an initial atomic state to a final state. If the final state lies in the continuum where the electron is no longer bound by the Coulomb potential, the electron is released and the atom becomes ionized. The outgoing electron can be characterized as an EWP with its wavefunction given as the sum of a bound state and a continuum part,

$$|\Psi(t)\rangle = a(t)\left|\tilde{i}\right\rangle + \int d^3(k) b(k,t)\left|\tilde{k}\right\rangle, \tag{2.11}$$

where $\left|\tilde{k}\right\rangle$ are the exact atomic states in the continuum and $\left|\tilde{i}\right\rangle$ the initial bound state. The probability of an EWP to be found in a continuum state is given by $|b(k,t)|^2$ with $b(k,t)$ being the transition amplitude. Experimentally, the probability amplitude is the observed quantity and can be calculated by inserting equation 2.11 into the TDSE which is presented in [9].

2.3.1   Photoionization in an IR dressed field

Several analytical models have been introduced to describe the photoionization by an XUV field and an IR dressing field [10, 23, 30]. The first full quantum-mechanical description of two-photon-transitions within the lowest order perturbation theory was based on a monochromatic approximation of the XUV and IR fields [10], but it is not suitable for our attosecond light source driven by few-cycle ultrashort pulses. A more recent model [23] accounts for the finite-pulse effect of Fourier transform-limited XUV pulses which is not the case for our attosecond pulses. Therefore, in this project, the well established Strong-field-approximation (SFA) [30] is used to describe the photoelectron amplitude.

Within a semi-classical description of the fields, the probability amplitude $a(\mathbf{p}_c)$ is given by the following expression based on first-order perturbation theory [24],

$$a(\mathbf{p}_c) = -i \int_0^t dt'\, \mathbf{E}(t) \cdot \mathbf{d}(\mathbf{p}_c)\, e^{i(S(\mathbf{p}_c,t,t_0)+I_p t)}. \tag{2.12}$$

In equation 2.12, the canonical momentum denoted by $\mathbf{p}_c$ is the conserved quantity which is defined as the sum of the classical momentum $\mathbf{p}$ and the vector potential of the laser field $\mathbf{A}(t)$. Additionally, $\mathbf{E}(t)$ represents the XUV electromagnetic field that ionizes the atom, I_p the ionization threshold, $\mathbf{d}(\mathbf{p}_c)$ denotes the dipole moment of the transition from the ground state to the continuum, and $S(\mathbf{p}_c,t,t_0)$ is the quasiclassical action related to the IR field given by

$$S(p,t,t_0) = \tfrac{1}{2}\int_{t_0}^t [\mathbf{p}_c]^2 = \tfrac{1}{2}\int_{t_0}^t dt'\left(p^2 + 2\mathbf{p}\cdot\mathbf{A} + \mathrm{A}^2(t)\right). \tag{2.13}$$

In general, in the SFA, the continuum states of the electron $\left|\tilde{k}\right\rangle$ are approximated by Volkov states $|k\rangle$ for which the spatial part of the wavefunction is defined by a plane wave [9]. The Volkov wavefunction is then given by

$$\langle \mathbf{r} | k \rangle = \frac{1}{(2\pi)^{3/2}} e^{i(\mathbf{k} + \mathbf{A}(t))\mathbf{r}} e^{-iS(\mathbf{p}_c, t, t_0)}, \tag{2.14}$$

and the dipole moment is expressed by $\mathbf{d}(\mathbf{p}_c) = \langle k | \hat{V}_I | \tilde{i} \rangle$.

In the context of this work, several approximations can be made. First, the experiments are conducted with a weak IR field such that $|\mathbf{A}| \ll \mathbf{p}$, hence, $S(p, t, t_0) = \frac{1}{2} \int_{t_0}^{t} dt' \, (p^2 + 2\mathbf{p} \cdot \mathbf{A})$. Assuming that the amplitude of the vector potential of the IR field is constant within one period of the optical cycle, it can be expressed as $\mathbf{A}(t) = \mathbf{A}_0 \cos(\omega(t - \tau))$ where τ is the fixed delay between the IR and the XUV field. Furthermore, in the particular case of this project, the electromagnetic field $\mathbf{E}(t)$ is an attosecond pulse train including a few pulses. Therefore, the total XUV electromagnetic field can be written as a sum over the field of every attosecond pulse $\mathbf{E}(t) = \sum_m \mathbf{E}_m(t)$ where m denotes the number of one attosecond pulse with $m = 0$ being the central pulse of the APT. Lastly, for helium ionization, the dipole moment $\mathbf{d}(\mathbf{p}_c)$ is approximated using a hydrogen atom [30], $\mathbf{d}(\mathbf{p}_c) \propto \mathbf{d}(\mathbf{p}) \propto \frac{\mathbf{p}(t)}{(\mathbf{p}^2(t)/2m_e + I_p)^3}$.

Under these considerations, the transition amplitude becomes

$$a(\mathbf{p}) = -i \, \mathbf{d}(\mathbf{p}) \cdot \sum_m e^{i\Phi_{IR}(\mathbf{p}, \frac{m\pi}{\omega})} \int_{-\infty}^{\infty} dt \, \mathbf{E}_m(t) \, e^{-i\Omega(t + \frac{m\pi}{\omega})} \tag{2.15}$$

where we assume that the phase induced by the IR field, Φ_{IR}, does not vary over the attosecond pulse duration. We replaced $\Omega = I_p + p^2/2$ where Ω describes the frequency range over which the photoelectron propagates. In order to simplify the transition amplitude even further, the induced IR phase Φ_{IR} is written as follows,

$$\Phi_{IR}(\mathbf{p}, \frac{m\pi}{\omega}) = \Phi_{IR}(\mathbf{p}, t) = \int_{t}^{\infty} dt' \mathbf{p} \cdot \mathbf{A}(t') = \frac{\mathbf{p} \cdot \mathbf{A}_0}{\omega} (-1)^m \sin(\omega\tau) \tag{2.16}$$

where the vector potential is defined as $\mathbf{A}(t) = (-1)^m \mathbf{A}_0 \cos(\omega(t - \tau))$. Since $\mathbf{p} \cdot \mathbf{A}(t)$ is weak, the induced IR phase term can be approximated by a Taylor expansion such that

$$e^{i\Phi_{IR}(\mathbf{p}, \frac{m\pi}{\omega})} \approx 1 - i\frac{\mathbf{p} \cdot \mathbf{A}_0}{\omega} (-1)^m \sin(\omega\tau). \tag{2.17}$$

Consequently, by inserting 2.17 into equation 2.15, the transition amplitude can be expressed as the sum of two contributions such that $a(\mathbf{p}) = a_1(\mathbf{p}) + a_2(\mathbf{p})$, where $a_1(\mathbf{p})$ and $a_2(\mathbf{p})$ are given by

$$a_1(\mathbf{p}) \approx -i\mathbf{d}(\mathbf{p}) \cdot \sum_m e^{i\frac{m\Omega\pi}{\omega}} \mathbf{E}_m, \tag{2.18}$$

$$a_2(\mathbf{p}) \approx -\frac{\mathbf{p} \cdot \mathbf{A}_0}{\omega}(-1)^m \sin(\omega\tau)\, \mathbf{d}(\mathbf{p}) \cdot \sum_m (-1)^m e^{i\frac{m\Omega\pi}{\omega}}\, \mathbf{E}_m. \qquad (2.19)$$

The first part describes the ionization by XUV attosecond pulses only while the second one represents the contribution from photoionzation by both XUV and IR pulses. In comparison with the experimental observations, we want to compute the probability amplitude $|\mathbf{a}(\mathbf{p})|^2$. Due to the sum, the computation of the probability amplitude will lead to the appearance of interference terms,

$$|a(\mathbf{p})|^2 = |a_1(\mathbf{p}) + a_2(\mathbf{p})| \cdot |a_1(\mathbf{p}) + a_2(\mathbf{p})|^* \qquad (2.20)$$

where the second term represents the complex conjugate of the sum.

2.3.2   Momentum Imaging

Three dimensional momentum imaging spectrometers provide unprecedented details of photoionization dynamics in atoms and molecules by measuring both the kinetic energy and the emission angle of charged particles [12]. These spectrometers are often referred to as Reaction Microscopes, since they allow us to analyze the products of a photoreaction. The working principle of these spectrometers is based on the fact that charged particle motion can be controlled with electrostatic and magnetostatic fields. Hence, after detection of the particle at a given position and time, it is possible to determine the particle momenta upon ionization by using the classical equation of motion [15]. Since the detection of ionic atoms usually does not pose a problem, only the detection of electron is discussed in the following.

In order to detect particles with 4π solid angle, a combination of electrostatic (E) and magnetostatic (B) fields, aligned along the spectrometer axis, is traditionally used. While the E-field allows for controlling the TOF and its spread, the B-field aims at confining the transverse motion of the electrons of kinetic energy, E_k, along a circle with a radius, R,

$$R = \frac{2\sqrt{2mE_k}}{qB}, \qquad (2.21)$$

so that all produced electrons reach the detector. With the help of the position and time-of flight on a detector (x,y,t), the initial momentum vector of the electron in the interaction region (where ionization occurs) can be determined. The transverse momentum component can be expressed as

$$\begin{bmatrix} p_x \\ p_y \end{bmatrix} = \frac{qB}{2} \cdot \begin{bmatrix} M(\omega t) & 1 \\ 1 & -M(\omega t) \end{bmatrix} \begin{bmatrix} x \\ y \end{bmatrix} \qquad (2.22)$$

where $M(\omega t) = csc(\omega t) + cot(\omega t)$ and $\omega = \frac{qB}{m}$ is the cyclotron frequency. As can be seen, this transformation has singularities every time $\omega t = n\pi$, which can be referred to as a magnetic node. The initial longitudinal momentum p_z can be expressed in its simplest form as,

$$\Delta p_z = qE(t - t_0) = qE\Delta t, \qquad (2.23)$$

where t_0 is the nominal time of flight for an electron with zero kinetic energy, and $\Delta t = 2\sqrt{2mE_k}/qE$ is the spread in time-of-flight, also referred as turn-around-time for electron emitted forward and backward with respect to the detector. The equations 2.23 and 2.22 imply that t_0 and Δt ought to be chosen properly to avoid consecutive magnetic nodes. By doing so, one can ensure that no three dimensional data information is lost during the analysis of an experiment.

At the beginning of this thesis work, a new spectrometer had recently been built based on the so-called CIEL design, which stands for 'Coincidences entre Ions et Electrons Localisés (i.e 'Coincidences between ions and electrons localised'). The originality of the design is to avoid magnetic nodes such that the time difference between two magnetic nodes, also referred to as the wiggling period of the magnetic field, T_w, is bigger than the turn-around-time,

$$T_w = \frac{2\pi m}{qB} > \Delta t, \tag{2.24}$$

by adjusting the geometry of the spectrometer. To achieve good resolution of the spectrometer, weak (E, B) fields are necessary. Consequently, any residual magnetic field, such as the earth field that might disturb the measurements, should be compensated as much as possible. Unfortunately studies discussing the resolution of 3D momentum spectrometer are scarce, which explains the necessity to study the limitation of our setup. Furthermore, according to the world magnetic model (WMM) [6] the vertical component of the magnetic field in Lund (47,43 μ T) is close to three times as big in magnitude as the horizontal component is (17 μ T). Unfortunately the first implementation of spectrometer was horizontal, i.e. perpendicular to the strongest component of the earth field, leading to many experimental constraints during the first experiment. A main part of the thesis aimed thus at changing the alignment of the spectrometer with respect to the earth field, i.e. from horizontal position to vertical position, and to perform a thorough study of the performance of the CIEL spectrometer with respect to the change.

Chapter 3

Experiment

In this chapter, the experimental details behind the photoionization experiment using attosecond pulses and the multiphoton ionization experiment to study the resolution of the spectrometer are presented. The helium photoionization experiment was conducted with an OPCPA laser system at a repetition of 200 kHz which provides IR pulses in the few-cycle pulse regime. After generating attosecond pulses, due to the low conversion efficiency of the generation process, both the attosecond XUV and the remaining IR laser fields are focused into an imaging spectrometer to create EWPs and their respective three-dimensional data set.

A plug-in for data analysis was programmed as an addition to a data analysis framework called ANACONDA2 developed in the group to provide a universal data analysis package for various coincidence spectrometer available in Sweden and France [4]. In this chapter, the main concepts behind the program is explained. The results generated with the help of the analysis framework are presented in chapter 4. In addition, a large part of the thesis work was to upgrade the mechanical holder in vacuum of the momentum imaging spectrometer, called CIEL as presented in chapter 2. This work included a design, commissioning phase and ultra-high vacuum tests. The overall work on the spectrometer took six months and details about the mechanical realization are presented in the appendix. Two experiments were conducted with the aim to study the spectrometer performance, in particular, the energy resolution before and after all changes have been implemented. In this chapter, we present the protocol behind the resolution study.

3.1   Principle of the attosecond experiment

The coincidence imaging spectrometer CIEL ("Coïncidences entre ions et électrons local-isés") was built within the group with the aim to measure ions and electrons in coincidence resulting from photoionization of atoms or molecules. The state-of-the-art high repetition rate attosecond light source based on the OPCPA technique can automatically achieve the coincidence regime through low pulse energies with not more than one ionization event per laser pulse. This system makes it possible to perform many coincidence light-matter-interaction experiments in the future. We report on the first one made at the time, when it was possible to only act on the CEP of the laser.
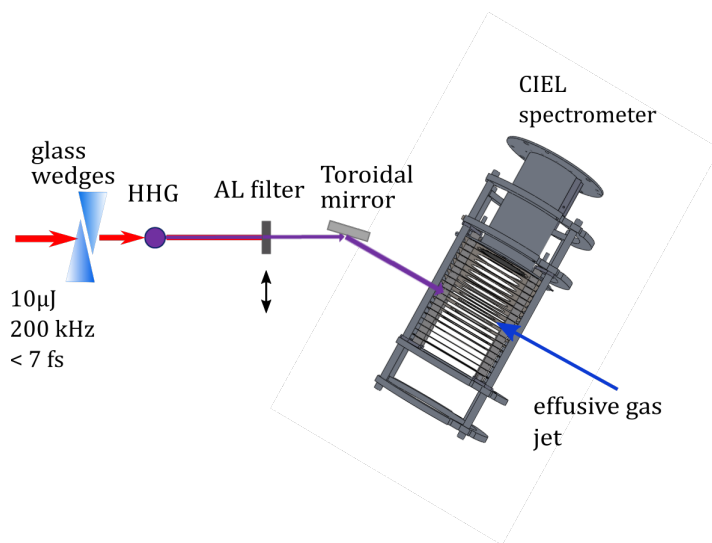

Figure 3.1.1: Illustration of the main components of the beamline used for the experiment on Helium. The IR laser field (in red) at a pulse energy of roughly 10 μJ and a pulse duration of less than 7 fs is used to generate attosecond pulses in a gas cell filled with argon (purple circle) through the process of HHG. The remaining IR can be filtered by placing an aliminium (Al) filter into the beam. A toroidal mirror focuses the beam into the CIEL spectrometer and an effusive gas jet lets the gas into the spectrometer. Two glass wedges can be inserted into the beam to change the CEP of the IR.

The principle of the experiment is illustrated in figure 3.1.1. The few-cycle IR pulses are provided at a repetition rate of 200 kHz with a duration below 7 fs and a pulse energy of approximately 10 μJ. These pulses, symbolized by red arrows, are then focused into an argon gas cell (purple ball) with a gas jet at a pressure of 10 bar. At intensities on the order of $10^{14} - 10^{15}$ W/cm^2, attosecond pulses are produced, here represented by a purple arrow. Since HHG has a rather low conversion efficiency, some IR signal is left after the generation. There is a possibility to filter out these IR pulses by placing and aluminium (Al) filter into the beam. Propagating through vacuum, the remaining XUV pulses are focused into the CIEL spectrometer (along the y-direction) with the help of a

toroidal mirror. Simultaneously, an effusive gas jet lets the detection gas enter the CAMP ("Chamber for Atomic and Molecular Physics") chamber from the x-direction. A typical working pressure in this chamber is 10^{-7} mbar. When the light pulses interact with the helium atoms, charged particles are created and collected by the detection apparatus of the CIEL spectrometer. This interaction changes with varying temporal characteristics of the attosecond pulses.
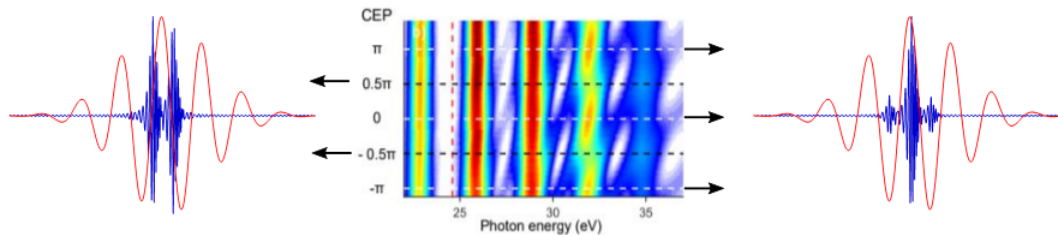

Figure 3.1.2: Scan of the XUV spectrum as a function of the CEP of the IR pulses from [7]. The CEP can be related to the glass insertion of the wedges. The red dashed line represents the ionization threshold of Helium at 24.6 eV. At an integer multiple of π, a white dashed line represents the experimental condition where the APT consists of 3 pulses. Likewise, at the black dashed line, the CEP is equal to a half-integer of π which corresponds to a condition in which the APT includes two attosecond pulses. By scanning the CEP, the two conditions are achieved.

Figure 3.1.2 represents how the XUV spectrum of the attosecond pulses changes with the CEP of the IR pulses beyond the ionization threshold of helium. In this experiment, the CEP of the IR pulses is varied with the help of two glass wedges. By varying the thickness of the glass inserted at the position of the incident beam, the dispersion and thus the CEP of the pulses is controlled [34]. Depending on the CEP, the temporal structure of the APT includes either an odd or an even number of pulses, represented by the black and white dashed line respectively. These are the two main cases studied within this thesis project.
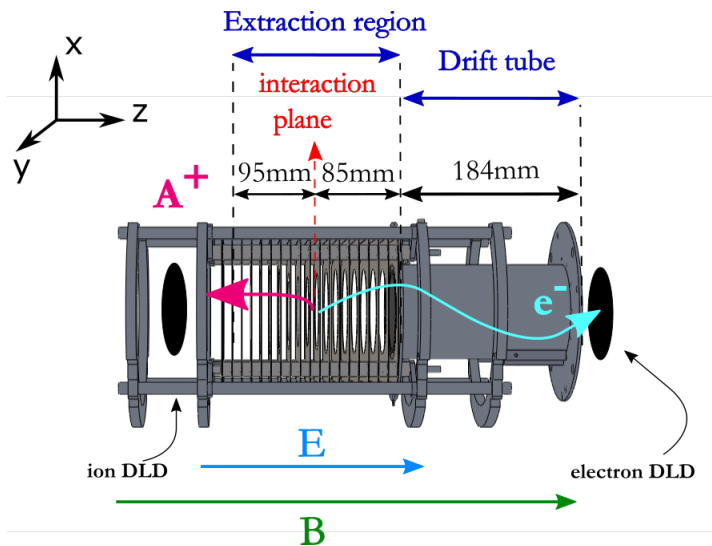
Figure 3.1.3: Illustration of the spectrometer working principle with the applied E and B fields along the main axis of the spectrometer shown in blue and green respectively. The produced electron e^- and ion A^+ during photoionization are represented in bright blue and pink. The interaction plane is plotted with a red dotted line while the extraction region (180 mm) and the drift tube (184 mm) are marked in blue. The two delay-line-detectors (DLDs) are shown in black for both electron and ion.

When the outlet of the effusive gas jet is correctly aligned to the laser focus, single photoionization events occur in the interaction plane of the CIEL spectrometer, which is divided into three parts, as shown in figure 3.1.3. In the first part, the extraction region, where the laser interacts with the gas, ions and electrons are directed into opposite directions, as introduced in chapter 2, thanks to an electric field **E**. To achieve a homogeneous electric field, 18 electrodes are placed over the extraction region. Additionally, the magnetic field **B**, necessary for 4π collection efficiency of electrons, is produced along the z-axis with the help of four magnetic coils. Two pairs of compensating coils control the B-field in transverse direction and can be used to compensate the Earth magnetic field. The second part of the electron spectrometer consists of a drift tube that allows us to control the electron TOF and to avoid magnetic nodes by adjusting the E- and B-fields [15]. Finally, the third part is related to the detection of the electrons by a delay-line-detector (DLD), shown here in black. Before being collected by the DLD, a charged particle needs to be amplified from 1 to 10^7 charges in order to obtain a good signal-to-noise-ratio for detection. Therefore, the electrons (or ions) first collide with a multichannel plate (MCP), installed before the DLD. Once amplified, an electron bunch is detected by the DLD and produces electronic signals. Once the electronic acquisition is initiated by a trigger signal, the analog electronic signals are further amplified and converted to the digital NIM standard (-0.8 V) which is then sent onto a Time-to-Digital Converter (TDC) [7]. While the MCP delivers the time-of-flight (TOF) t value of the charged particle, the DLD serves to determine the two-dimensional final position x, y of the particles on the detector. With the help of these

three coordinates, the initial three dimensional momentum vector $\mathbf{p} = (p_x, p_y, p_z)$ of the electrons can be reconstructed using equations 2.22 and 2.23.

3.2   Data Analysis

The three dimensional raw data x, y, t collected with the CIEL spectrometer do not yet provide information about the kinematics of the photoionization reaction. The raw data needs to be converted in order to analyze the photoelectron energies. For this purpose, an object oriented program called ANACONDA2 (ANAlysis of COiNcidence DAta) is used. In this section, the structure and principle behind the data analysis program is explained.

3.2.1   Anaconda 2

ANACONDA2 is an object oriented package in Matlab initiated in the group. The long-term goal of this software is to create a universal data analysis tool which can widely be used at research facilities. It saves time and the need to write basic routines for analysis and visualisation. During this work, a plug-in for the CIEL spectrometer is written which includes the specific equations necessary to convert raw data from the CIEL. In parallel to the source code, the graphical user interface (GUI) was updated by adding a calibration tool. A GUI is user-friendly and does not require detailed knowledge of the source code.

Every acquisition starts with a trigger signal which is referred to as an *event*. In case of the CIEL spectrometer, both a signal from a photodiode and the ion signal of the DLD can be used to initiate a trigger signal. Each *hit* on the ion or electron detector during an *event* is labelled as a number and saved in a vector where each row corresponds to one *event*. If no *hit* is registered during an *event*, 'NaN' is saved as an entry. If two *hits* were experienced during the previous *event*, the integer number on the current event is increased by two. After restructuring the raw data according to *hits* and *events*, the analysis can be started.
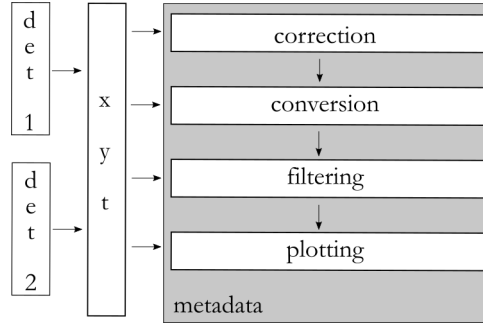
Figure 3.2.1: Data analysis principle behind the Anaconda acquisition program. The raw data x,y,t from both the electron detector (det1) and the ion detector (det2) is structured in data arrays and expressed in units of mm for position and ns for TOF. The program gives the option to correct, convert, filter and plot the data. Throughout all these steps, a metadata structure defines the conditions of these operations.

Figure 3.2.1 illustrates the main steps of the data analysis in the ANACONDA2 package. The first step is to save all raw data into a separate structure for the electron and ion detector. Afterwards, the program analyzes the data by following four main steps: Correction, conversion, filtering and plotting. The correction redefines all raw position and TOF data through the substraction of an offset, such that

$$
\begin{aligned}
x &\rightarrow x - \Delta x, \\
y &\rightarrow y - \Delta y, \\
t &\rightarrow t - \Delta t.
\end{aligned}
\tag{3.1}
$$

The position offset can be due to many reasons. For instance, the effusive needle might not be ideally positioned at the center of the detectors. If necessary, there is also an option to correct for rotational misalignment of the detectors. Furthermore, a misalignment of the E- or B field could also cause the position to vary. Likewise, the trigger signal might have a slight offset of a few ns which needs to be corrected. After having performed the correction of the raw data arrays, the conversion from position and TOF to momentum can be started. Thereby, equations 2.22 and 2.23 are used. The time offset as well as the magnetic and electric field values can be modified in order to obtain a centered and circularly shaped momentum signal. During the analysis, it is noted that the linear approximation made in equation 2.23 was not always be valid. The expression for the momentum in z-direction can therefore be extended by higher order correction terms of $(t - t_0)$. From the calibrated momentum, the kinetic energy is calculated by

$$
E_k = \frac{|p|^2}{2 \cdot m}
\tag{3.2}
$$

where m is the mass of the examined particle. Since the kinetic energy has a quadratic dependence on the momentum, any miscalibration in momentum creates a greater miscalibration in kinetic energy. Moreover, the momentum can be converted to a different spatial

representation which is discussed in the 'data representation' section. Finally, different filters can be applied to the data arrays and both the corrected raw data and the converted data arrays can be plotted.

All quantative values which are needed for correction, conversion, filtering and plotting are defined in a metadata file which can be redefined for every new data set. In the metadata, it is also defined which data analysis steps are executed for both detectors. For example, most often we are only interested in the electron energy distribution and only use the ion X-Y plot as a reference for filtering. Consequently, it is not necessary to convert the ion raw data to momentum and kinetic energy. Furthermore, the metadata defines which data arrays are contained in the different plots and whether the plot is executed or not.

3.2.2 Data representation

The three dimensional momentum is represented in spherical coordinates with a magnitude $|\mathbf{p}|$, an azimuthal angle ϕ and a spherical polar angle θ which are defined as follows from the momentum in a cartesian coordinate system [19],

$$|\mathbf{p}| = \sqrt{p_x^2 + p_y^2 + p_z^2},$$
$$\theta = \tan^{-1}\left(\frac{p_y}{p_x}\right), \qquad (3.3)$$
$$\phi = \cos^{-1}\left(\frac{p_z}{|\mathbf{p}|}\right).$$

The spherical polar angle θ reaches from 0 to π and the azimuthal angle from 0 to 2π as shown in figure 3.2.2.
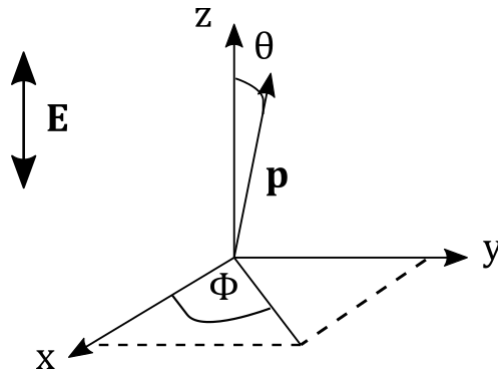

Figure 3.2.2: Spherical coordinate system with three dimensions coordinates $\mathbf{p}$, θ and ϕ drawn in the cartesian coordinate system with x,y and z axes.

There are different ways to represent the momentum data, and we choose a representation that allows for the highest statistics as possible which is achieved through azimuthal

integration. The integrated data are plotted in two dimensions with the momentum in z-direction p_z and the momentum along the x-y plane p_r. Both of them are redefined through the spherical coordinates such that

$$p_z = |\mathbf{p}| \sin(\theta),$$
$$p_r = |\mathbf{p}| \cos(\theta). \tag{3.4}$$

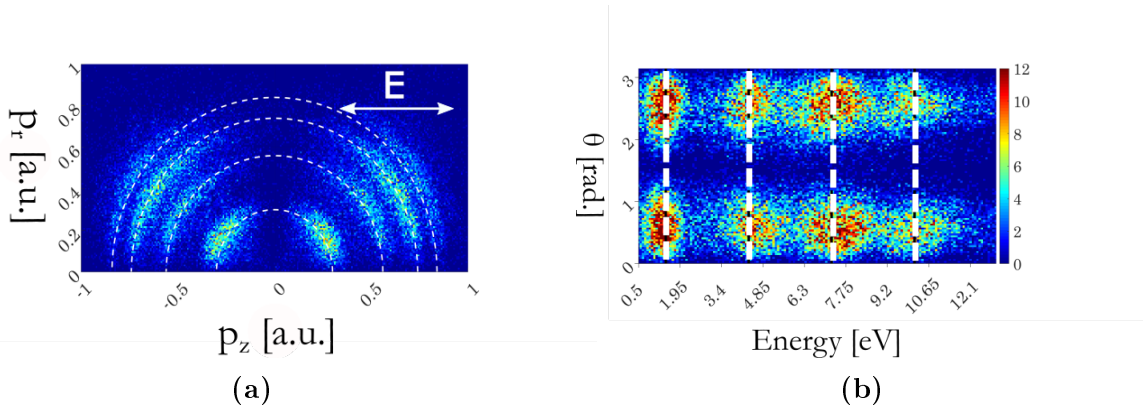(a)   (b)

Figure 3.2.3: Data representation of photoelectron converted data. (a) 2D momentum representation with transverse momentum p_r plotted against the momentum p_z which is parallel to the electric field polarization **E**.(b) Kinetic photoelectron energy plotted along the spherical polar angle

Figure 3.2.3 (a) and (b) show the photoelectron momentum and energy signals from a photoionization experiment where helium atoms are ionized with attosecond XUV pulses produced by HHG. Each 'half-ring' in the momentum figure corresponds to a photoelectron emitted after absorption of an odd harmonic frequency of the laser field. Since the laser is polarized along the z-axis, the photoelectrons only propagate along this axis and no signal is observed around the area where $p_z = 0$. We can identify that the momentum is well calibrated based on two features. First, the rings are centered with respect to the p_z origin and secondly, they can be fitted to a circular shape, plotted here as a white dotted line. The photoelectron kinetic energy converted from the momentum is shown in figure 3.2.3 b. As expected, the photoelectron energies lie at odd multiples of 1.5 eV originating from the absorbtion of odd harmonics. Consequently, the spacing between the energy peaks equals roughly 3 eV. The signals are rather straight and not tilted which implies a good calibration. Moreover, the signal is symmetric along the polarization direction. In the following parts of the thesis work, we will essentially represent the photoelectron energy as in Fig. 3.2.3.

3.3 Resolution and calibration study

As part of the resolution study within this work, an experiment was set up and the collected data were analyzed. In this section, the experimental details as well as the concept of energy resolution are presented. The results are then discussed in chapter 4.

3.3.1 Principle of the experiment

The resolution experiments are conducted with the Pharos laser system with pulse energies varying between $200 - 340\,\mu$ J, at a wavelength of 1030 nm [32] and a repetition rate of 20 kHz. Compared to the OPCPA laser pulses, this Pharos laser output is advantageous to study the energy resolution because the pulse duration of 170 fs provides a narrow spectral linewidth.

The pulses are focused into the CIEL by a simple lens of focal length f=43 cm, installed in front of the chamber. At a focus size of $135\,\mu$m^2 at the gas target, intensities on the order of 10^{13} W/cm^2 are reached. This intensity regime allows for above-threshold-ionization (ATI) in heavy rare gases like Krypton [1]. ATI results from the absorption of several photons in order to reach energy levels above the ionization threshold I_p from the ground state energy, E_i, of the gas atoms which is illustrated in figure 3.3.1 below. Thereby, the photoelectron energy signals are observed at energies corresponding to the following values,

$$E_n = (n + m)\hbar\omega - I_p \qquad (3.5)$$

where m represents the mimimum number of photons that need to be absorbed to reach the threshold energy I_p and n is any integer of photons being observed after the threshold.
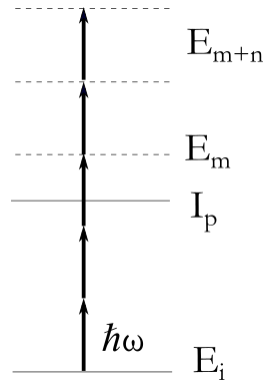

Figure 3.3.1: Illustration of ATI principle with an initial energy ground state E_i and energy states at multiple photon energies of $\hbar\omega$ above the ionization threshold I_p

The energy peaks are separated by one photon energy $h\nu_{IR}$ which is approximately equal to 1.2 eV in the ATI experiment due to the operating wavelength of 1030 nm. The clear spacing between the photoelectron energy peaks and the more narrow bandwidth makes the ATI experiment most suitable for energy resolution analysis in our case in comparison

to photoionization by attosecond pulses. The same laser parameters and experimental setup are used to calibrate the magnetic field of the spectrometer.

3.3.2   Calibration

First of all, for the magnetic field calibration produced by the main coils, a condition needs to be found where magnetic nodes start appearing. The magnetic nodes can be found by adjusting the voltage on the electrodes, i.e. by decreasing the electric field to $2-3.5$ V/cm. Consequently, the photoelectron pattern will move. Once the pattern covers two magnetic nodes, their wiggling period in the magnetic field T_w is read from a plot and the same is repeated for several current values applied to the main coils. With the help of equation 2.24, the wiggling period can be converted to a magnetic field value and plotted with respect to the applied current. Finally, a linear fit defines the magnetic field dependence on the applied voltage.

Figure 3.3.2a shows the electron TOF as a function of its position on the DLD x-axis. It is clearly shown that the ATI pattern covers three magnetic nodes which are located at the three red dotted lines where there are no data points along the position axis. The nodes are separated in time by two wiggling periods and their average provides the final wiggling period T_w, thus the magnetic field value B. The applied current to the magnetic coils is varied from 2.6 to $4A$.

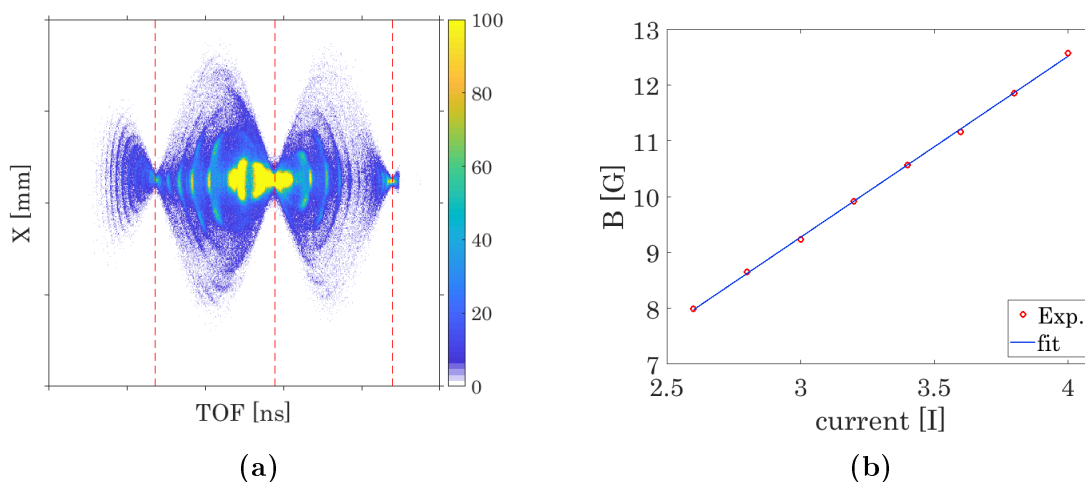(a)   (b)

Figure 3.3.2: (a) ATI pattern plotted in a TOF-X plot with three magnetic nodes (red dotted line) as a function of position X with two magnetic nodes at a setting of $350\mu J$ and 20 kHz. (b) Magnetic field value in Gauss as a function of applied voltage to the main coils when the horizontal compensating coils are switched on. The spectrometer operates with weak a extracting field 2-3.5 V/cm.

Figure 3.3.2b shows the obtained magnetic field values for each applied current. After fitting a linear function to the experimental data points, we can describe the evolution of

the magnetic field in Gauss ($1\text{G} = 10^{-4}$ T) by

$$B = 3.24\,\text{I} - 0.4510. \tag{3.6}$$

The first term of the above equation is related to the magnetic field created through induction by the main coils. The second term represents the contribution of the Earths magnetic field as can be confirmed by comparing it to the vertical magnetic component of $47\,\mu\text{T}$.

3.3.3   Resolution

Energy resolution is defined as the accuracy at which two closely lying energy values can be distinguished [29]. This accuracy translates into how precisely the collected experimental data can be analyzed. It can be defined as the relative resolution $\frac{\delta E}{E}$ where δE is the full width at half maximum (FWHM) of a gaussian fit at every energy peak [25] or the absolute resolution value ΔE_k . The experimental energy deviation can be modelized as follows [7],

$$\Delta E_{exp}(x,y,t) = \sqrt{(\frac{\partial E_{exp}}{\partial x})^2\sigma_x^2 + (\frac{\partial E_{exp}}{\partial y})^2\sigma_y^2 + (\frac{\partial E_{exp}}{\partial t})^2\sigma_t^2} \tag{3.7}$$

where σ_x, σ_y, and σ_t represent the size of the interaction volume in x and y dimension and the temporal detector response respectively. After computation of each partial derivative, the full expression is given by

$$\Delta E_{exp}(x,y,t) = \sqrt{A(x^2 csc^2(\frac{\omega t}{2}))\sigma_x^2 + A(y^2 csc^2(\frac{\omega t}{2}))\sigma_y^2 + (\frac{p_z}{m}\frac{\partial p_z}{\partial t} - B(cot(\frac{\omega t}{2})csc(\frac{\omega t}{2})))^2\sigma_t^2} \tag{3.8}$$

where $A = \frac{m^2\omega^4}{16}$, $B = \frac{m\omega^3}{8}r^2$, and ω is the cyclotron frequency of the magnetic field. Equation 3.8 shows that the energy resolution depends on the source volume, the temporal response of the detectors, but also on the quality of the magnetic field alignment due to the dependence on ω. The resolution study is done to verify how these factors influence the energy measurement in horizontal and vertical orientation of the spectrometer. When computing the resolution in equation 3.8, the E and B fields from the final experiment at vertical configuration are used as a reference. From the same experiment, the corrected raw data (x,y,t) after filtering on an interaction volume with size $\sigma_x \times \sigma_y$ is used. Also note that the energies in the simulation of 3.8 are integrated along the polar angle. In addition to equation 3.8, the intrinsic linewidth of the above threshold ionization (ATI) experiment needs to be taken into account [25]. Thus, the total expression for the energy deviation becomes

$$\Delta E_k = \sqrt{(\Delta E_{exp})^2 + (\Delta E_{ATI})^2}. \tag{3.9}$$

Chapter 4

Results and Discussion

In this chapter, we start by discussing the results obtained from the photoionization experiment in Helium with XUV attosecond pulses and an IR dressing field, and then we present the multiphoton ionization experiment for calibration and resolution purposes.

4.1 Photoionization of Helium

This section presents the observations made in the Helium photoionization experiment and finally divides the observations into two main parts which are analyzed with the help of an analytical model.
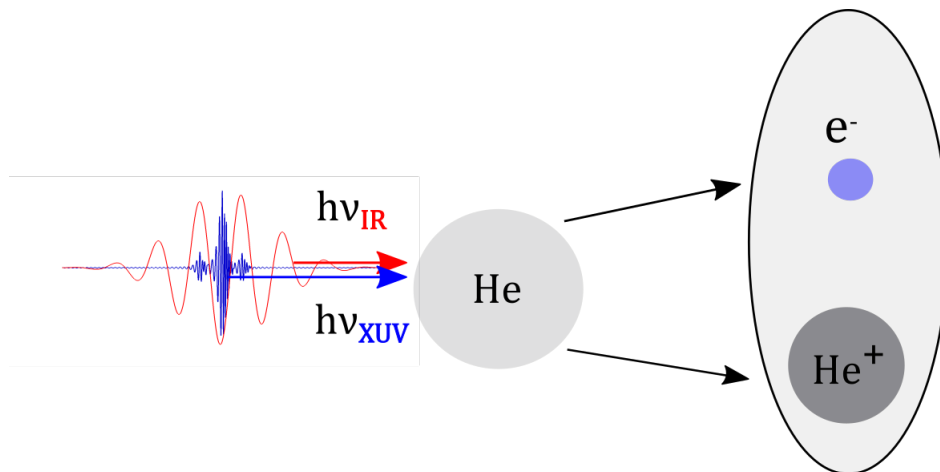

Figure 4.1.1: Illustration of photoionization of Helium (He): $He + h\nu_{\mathrm{IR}} + h\nu_{\mathrm{XUV}} \rightarrow He^+(1s) + e^-(l\epsilon)$ where $l = 1$ for XUV only and $l = 0, 2$ for XUV and IR. The IR photons are represented with a red arrow and the XUV photons in blue.

Figure 4.1.1 serves as a reminder of the principle of photoionization. XUV photons produced by HHG carrying an energy $h\nu_{\mathrm{XUV}}$ greater than I_p interact with helium atoms 'He'. As a result, an EWP is released, leaving a positively-charged helium ion. During

the experiments, the XUV photons are overlapped with the initial IR dressing laser field, represented in red by $h\nu_{IR}$. The parity of the outgoing electron wave packet changes, depending on whether only XUV pulses or the combination of both XUV and IR pulses are used. We choose to study helium due to its simple atomic structure with only two electrons in the ground state ($1s^2$). After photoionization, the three dimensional raw data of both electron and ion are collected, converted to momentum with the help of the equations presented in chapter 2, and finally converted to kinetic energy.
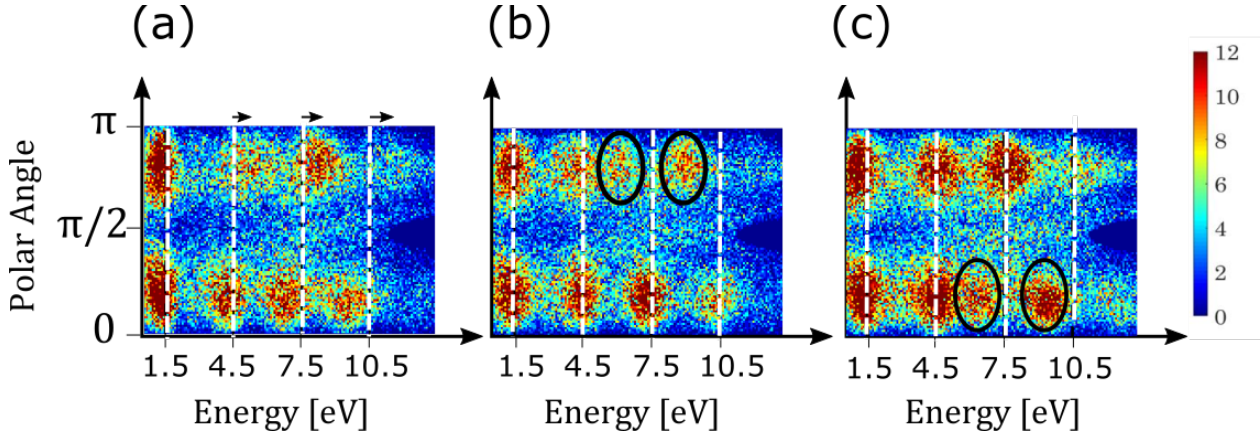

Figure 4.1.2: Photoelectron energy distribution as a function of energy and polar angle at three different CEP values: (a) at $\varphi = \pi/2$ with a shift of the photoelectron peaks indicated by black arrows, (b) at $\varphi = \pi$ with two sidebands appearing above a spherical polar angle of $\pi/2$, (c) at $\varphi = 0$ with sidebands appearing below a spherical polar angle equal to $\pi/2$. The white dashed lines correspond to the EWP energies emitted after absorption of odd harmonics only with a clear separation of around $2h\nu_{XUV} = 3$ eV.

In figure 4.1.2 the photoelectron energy distribution is shown as a function of kinetic energy and polar angle based on the definition in equation 3.3. The leftmost figure 4.1.2 (a) is obtained when the CEP of the IR is set to $\pi/2$ and the APT consists of two attosecond pulses. In this photoelectron distribution, we see a shift of the photoelectron peaks with respect to the energy peak values obtained in the case of photoionization by XUV pulses only, which is marked by dashed white lines. For polar angles greater than $\pi/2$, the peaks shift towards higher energies, while below $\theta = \pi/2$, the peaks are shifted towards lower energies.

In figure 4.1.2 (b) and (c), the results are shown at a CEP of 0 and π respectively. In both cases, three attosecond pulses are generated, but the direction of the IR field is reversed for the rightmost figure. For the photoelectron distribution in fig. 4.1.2 (b), we observe that the energy peaks are situated at the same energy values as for the XUV-only case at polar angles smaller than $\pi/2$. On the contrary, for polar angles larger than $\pi/2$, new peaks start appearing in between the white dashed lines, also referred to as 'sidebands'. When the IR field changes sign in fig. 4.1.2, this situation is reversed with respect to the polar angle at $\pi/2$.

The next sections explain how the addition of the IR field in the photoionization process creates a variance in the photoelectron spectrum. An analytical model expresses the observations made in the cases of two and three pulses and finally, an analogy to the slit experiment is provided.

4.1.1 Two Pulses

In order to gain a better understanding of the angle-resolved kinetic energy signal obtained from the experiment in figure 4.1.2 (a), the photoionization transition amplitude in a dressed field is simulated based on the SFA model presented in chapter 2. In this case, the APT comprises two attosecond pulses. The result of the simulation is shown below.
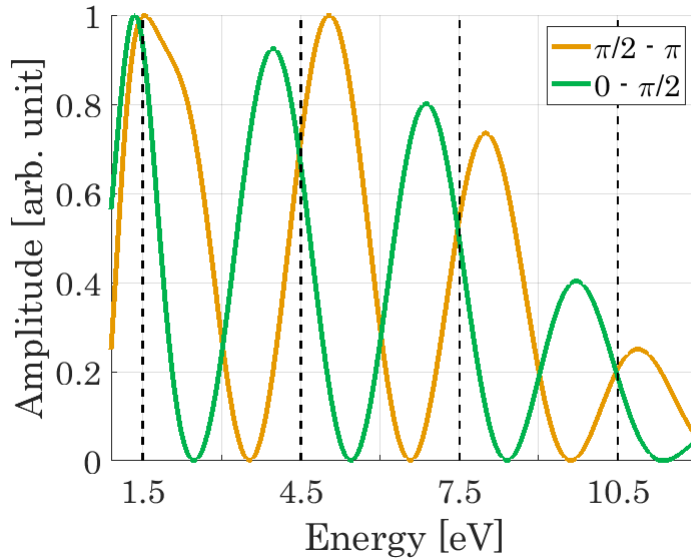

Figure 4.1.3: SFA simulation of the photoionization probability amplitude $|\mathbf{a}(\mathbf{p})|^2$ at a CEP equal to $\pi/2$ with an APT made of two pulses. The integration range corresponds to $\pi/2 - \pi$ in orange with a shift to higher energy values and to $0 - \pi/2$ in green with shifts to lower energy values. This simulation corresponds to the experimental figure 4.1.2(a). The energy peak values from the SFA simulation at XUV pulses only are represented by black dashed lines.

Figure 4.1.3 above illustrates the photoionization probability amplitude in an IR dressing field, $|\mathbf{a}(\mathbf{p})|^2$, at a CEP equal to $\pi/2$. The orange and the green curves represent the simulated photoelectron distribution taking into consideration the experimental conditions in figure 4.1.2 (a), integrated from a polar angle of $\pi/2$ to π, and 0 to $\pi/2$ respectively. We can see that the simulation replicates the experimental result.

With the help of an analytical derivation carried out as part of this work, the physical origin of this shift can be understood. From chapter 2, we know that the photoelectron transition amplitude $a(\mathbf{p})$ can be divided into two contributions $a_1(\mathbf{p})$ and $a_2(\mathbf{p})$ which are

given by

$$a_1(\mathbf{p}) \approx -i\mathbf{d}(\mathbf{p}) \cdot \sum_m e^{i\frac{m\Omega\pi}{\omega}} \mathbf{E}_m(\Omega), \qquad (4.1\text{a})$$

$$a_2(\mathbf{p}) \approx -\frac{\mathbf{p} \cdot \mathbf{A}_0}{\omega}(-1)^m \sin(\omega\tau)\mathbf{d}(\mathbf{p}) \cdot \sum_m (-1)^m e^{i\frac{m\Omega\pi}{\omega}} \mathbf{E}_m(\Omega), \qquad (4.1\text{b})$$

where the XUV field is expressed as the sum over m pulses. In the case of two pulses, m is set to 0 and 1 for the first and second pulse. We assume that the pulse at $m = 0$ has a zero spectral phase and that the second pulse with respect to the first one has a π phase offset. Both pulses have a maximum amplitude equal to 1, such that $\mathbf{E}_m = 1 + e^{i\frac{\Omega\pi}{\omega}+i\pi}$. Hence, by using the property that the sine function can be expressed as a sum of exponential terms, the expressions are rewritten as

$$\begin{aligned}
a_1(\mathbf{p}) &\approx -2\,\mathbf{d}(\mathbf{p}) \cdot \mathbf{E}_0(\Omega)e^{\frac{i\pi\Omega}{2\omega}} \sin\left(\frac{\Omega\pi}{2\omega}\right) \\
a_2(\mathbf{p}) &\approx -2\,\eta_p\mathbf{d}\,(\mathbf{p}) \cdot \mathbf{E}_0(\Omega)e^{\frac{i\pi\Omega}{2\omega}} \sin\left(\frac{\Omega\pi}{2\omega}\right)
\end{aligned} \qquad (4.2)$$

where $\eta_p = \frac{\mathbf{p} \cdot \mathbf{A}_0}{\omega}(-1)^m \sin(\omega\tau)$. By summing the two terms according to equation 2.20, the total transition amplitude is given by

$$|a(\mathbf{E})|^2 \propto \sin^2(\frac{\pi\Omega}{2\omega} + \eta_p). \qquad (4.3)$$

This equation describes a periodic oscillation as a function of the frequency Ω, thus the photoelectron energy. The second term, η_p, indicates a phase offset which depends on the momentum $\mathbf{p}$ and the IR field amplitude $\mathbf{A}(t)$. When η_p is zero, the maximum transition amplitude is found at odd multiples of ω such that $\Omega = (2n+1)\omega$, which is what we expect from the XUV-only case. However, when $\eta_p \neq 0$, the maxima of the transition amplitude are shifted proportionally to the magnitude of η_p. Since η_p is proportional to $\mathbf{p} \cdot \mathbf{A(t)}$, the shift depends first of all on the direction of the momentum, i.e. the sign of p_z. When the photoelectrons are emitted in the negative z-direction, they experience a negative phase offset, $-\eta_p$, which results in a shift towards higher energy values. The emission along the negative z-axis corresponds to a polar angle close to π. By changing the momentum direction, η_p becomes positive and instead, the peaks shift towards lower energies. A similar effect is observed when the IR field amplitude $\mathbf{A}(t)$ is reversed. However, now the direction is reversed, with shifts towards higher energies at positive p_z and towards lower energies for negative p_z. This scenario would correspond to a π shift of the CEP, hence a CEP equal to $-\pi/2$. In conclusion, we can observe an asymmetry in the photoelectron kinetic energy distribution with respect to the emission direction and the direction of the IR field.

4.1.2   Three Pulses

Similar to the two pulse case, an SFA simulation together with an analytical derivation explains the appearance of sidebands in the photoelectron energy distribution when the APT is composed of three attosecond pulses.
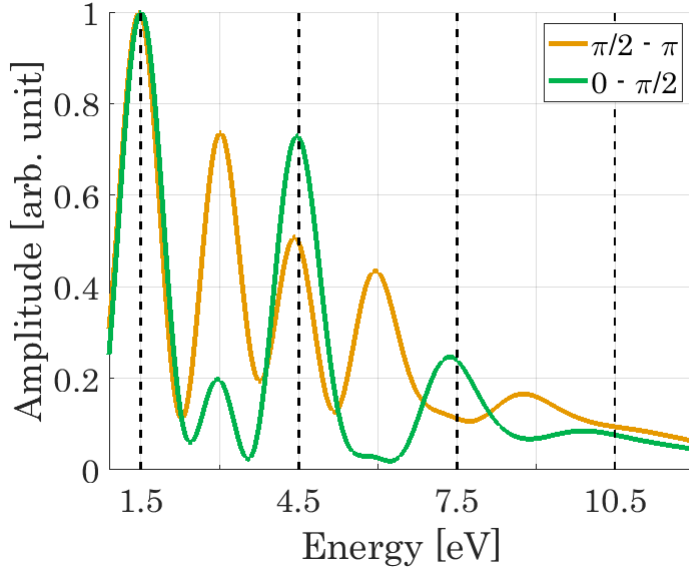
Figure 4.1.4: SFA simulation of the photoionization transition amplitude $\mathbf{a}(\mathbf{p})$ at a CEP equal to 0 with an APT made of three pulses. The integration range corresponds to $\pi/2 - \pi$ in orange with sidebands appearing at 3 eV and 6 eV, and to $0 - \pi/2$ in green with no sidebands appearing at those energies. This simulation corresponds to the experimental figure 4.1.2(b). The energy peak values from the SFA simulation at XUV pulses only are represented by black dashed lines.

Based on the analysis of the two-pulse-case, we know that a polar angle above $\pi/2$ can be interpreted as a negative emission direction and as a positive emission direction below $\pi/2$. At a CEP equal to 0, figure 4.1.4 shows the simulated transition amplitude for a negative and positive emission direction in orange and green respectively. For a mathematical expression of the XUV field at three attosecond pulses, the central pulse corresponds to $m = 0$ with a zero phase and the two sidepulses $m = 1$ and $m = -1$ are phase shifted by π and $-\pi$ with respect to the middle pulse. After inserting the development of the sum over the m pulses $\mathbf{E}_m = 1 + e^{i\frac{\Omega\pi}{\omega}+i\pi} + e^{i\frac{\Omega\pi}{\omega}-i\pi}$ 4.2, the amplitudes $a_1(\mathbf{p})$ and $a_2(\mathbf{p})$ can be rewritten as 4.2

$$a_1(\mathbf{p}) = -id_\epsilon(\mathbf{p})E_0(\Omega)\left(1 - 2e^{is}\cos\left(\tfrac{\Omega\pi}{\omega}\right)\right) \tag{4.4a}$$

$$a_2(\mathbf{p}) = -\eta_p d_\epsilon(\mathbf{p})E_0(\Omega)\left(1 + 2e^{is}\cos\left(\tfrac{\Omega\pi}{\omega}\right)\right) \tag{4.4b}$$

where s is the phase difference between the outer and the middle pulse. Following the same step as for two pulses, the transition amplitude in the three-pulse-case can be approximated by

$$|a(\mathbf{p})|^2 \propto 1 + 4\cos\left(\frac{\Omega\pi}{\omega}\right)^2 - 4\cos\left(\frac{\Omega\pi}{\omega}\right)\cos(s - 2\eta_p). \tag{4.5}$$

This phase difference is related to the fact that the middle pulse is generated at a different intensity than the two outer pulses. Compared to the two-pulse case, this analytical

expression includes three terms, with the first one being a constant equal to 1. Therefore, the amplitude in the cases of three pulses never completely becomes zero while it does in the case of two pulses as can be seen by comparing figure 4.1.3 and 4.1.4. The second term is an oscillation as a function of Ω, thus energy, with an amplitude of 4. This term has its maxima at any multiple of π such that $\Omega = n\omega$, i.e. at all harmonics of the fundamental frequency. The last part of the equation is a product of two cosine signals with a negative amplitude of 4r. The first cosine function oscillates again as a function of Ω, however, with positive maximum positions at even harmonics and minimum positions at odd harmonics. The second cosine phase depends on the difference between the phase offset s and the introduced phase offset by the IR field, η_p. Analyzing this equation step by step helps to understand the physical origin of the sidebands.

We first consider the case with no additional IR phase, $\eta_p = 0$, and $s = 0$. Since now $\cos(s - 2\eta_p) = 1$, the third term becomes a single cosine function depending on Ω. Without the contribution of this third term, we would observe peaks at energies corresponding to both odd and even harmonics, i.e. both at the black dashed lines and in between. However, since at even harmonics of ω the term $-4\mathrm{r}\cos\left(\frac{\Omega\pi}{\omega}\right)$ is negative, it cancels the peaks at those positions, which we call sidebands. Thus, we recapture the expected signal at XUV pulses only.

In a second scenario, the IR phase is added to the analysis, such that $\eta_p \neq 0$ and $s = 0$. Therefore, the third term in the equation 4.5 is modulated by the cosine function $\cos(-2\eta_p)$. As this cosine oscillation varies slowly with momentum $\mathbf{p}$, it can be understood as a constant factor, with a maximum value of 1, that reduces the strength of last term. From the analysis of two pulses, we know that the IR phase depends on the emission direction. Therefore, the strength modulation of the last should depend on the sign of the IR phase. However, since cosine is an even function, it does not vary with the sign of η_p. Hence, there is no asymmetry caused by the addition of the IR phase.

Finally, we look at the situation where $\eta_p \neq 0$ and $s \neq 0$. Now, the amplitude of the third term is modulated by $\cos(s - 2\eta_p)$ which increases or decreases the sideband signal. In this case, the sign of the IR phase offset η_p plays a role as it can influence the absolute value of $s - 2\eta_p$. Therefore, the addition of the attochirp contribution s is the factor that creates the asymmetry along the emission direction in the case of three pulses.

This analysis is limited to hydrogen-like atoms where a single photoionization path is considered and the dipole moment $\mathbf{d}(\mathbf{p})$ is approximated by a hydrogenic model. For more complex atoms, the dipole moment needs to be redefined and the SFA model needs to be developed further.

4.1.3   Interpretation

In this section, we show that the electron-wave-packet interference that we analytically explained in the two previous sections is related to a Fraunhofer slit experiment. We start

by recalling the expression of the transition amplitude from chapter 2,

$$a(\mathbf{p}) = -i\,\mathbf{d}(\mathbf{p}) \cdot \sum_m e^{i\Phi_{IR}(\mathbf{p},\frac{m\pi}{\omega})} \int_{-\infty}^{\infty} dt\,\mathbf{E}_m(t)\,e^{-i\Omega(t+\frac{m\pi}{\omega})}. \tag{4.6}$$

One can recognize that the integral in this expression corresponds to the Fourier transform of the XUV field. Consequently, the photoionization transition amplitude can be reformulated as

$$a(E) \propto \sum_m \int dt A_m(E,t)e^{-i\frac{E}{\hbar}t} \tag{4.7}$$

where $A_m(E,t) \propto \mathbf{d}(\mathbf{p}) \cdot e^{i\Phi_{IR}(\mathbf{p},\frac{m\pi}{\omega})}\mathbf{E}_m(t)$ and $E = I_p + p^2/2m$. This formulation is comparable term by term to the Fraunhofer diffraction principle with slits in the near field, described by the complex amplitude $A_m(E,t)$. In the far field, the diffracted light from the slits is observed as the Fourier transform of this complex amplitude [41]. In this analogy, the EWPs generated by the attosecond pulses in a presence of the dressed field in the time domain represent the slits in our experiment. The diffraction pattern in the far field corresponds to the signal we observe in the energy domain.
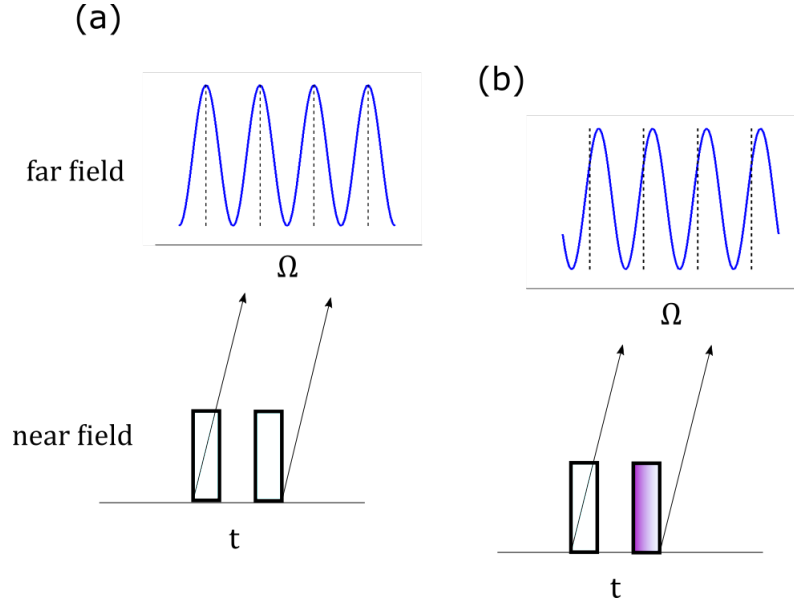

Figure 4.1.5: Slit experiment illustration with two slits in the time domain or near field representing the EWPs and their Fourier transform in the frequency domain representing the main features of the photoelectron energy signal in the far field: (a) Two slit experiment analogy to photoionization with only XUV pulses, (b) Two slit experiment analogy to photoionization with an IR dressing field that shift the frequency pattern away from the peak values in case (a).

In the case of two attosecond pulses, we look at an experiment with two slits. Figure 4.1.5 shows that the EWPs created by XUV pulses only create an interference pattern in

the far field with peaks at odd harmonics. The introduction of an additional IR field is analogous to the introduction of a phase plate [41] in one of the slits. The phase plate can be interpreted as the movement of one slit with respect to the other, therfore the diffracted light from the two slits does not interfere constructively at the same points in the far field anymore and we observe a shift in the energy peaks. When the phase plate is positioned in the other slits, the shift changes direction.

In the case of three attosecond pulses and three slits, we observe interference between the diffraction patterns of each adjacent slit and between the pattern from the two outermost slits. The former interference occurs when the middle slit is removed and results in peaks appearing at energies corresponding to both odd and even harmonics, i.e. including sidebands. This process can be referred to as intercycle interference, i.e. two slits from different subcycles interfere. When the middle slit is put back, two slit signals from the same cycle interfere which we refer to as intracycle interference. This interference between each pair of adjacent slits creates additional peaks at odd harmonics and thereby enhances the signal at odd harmonics. Consequently, the case at XUV pulses only is reproduced. The introduction of a phase plate in the middle slit causes a shift of the intracycle interference pattern similar to the two pulse case. Hence, the signal at odd harmonics becomes stronger again.

The addition of the phase offset s to the two outermost pulses can be interpreted as a shift of the slits away from the central slit, or closer to it depending on the emission direction which causes the asymmetry. In our experiment, this phase is related to the term $\kappa(\Omega)$ of the attosecond pulse phase in equation 2.7 which becomes more important at short pulses, as we have.

Overall, for two slits, the shift of photoelectron peaks resembles the streaking method [14] widely used in the attosecond community to characterize the duration of SAP. On the other hand, for three slits, thanks to intercycle interference, sidebands start appearing in between odd harmonics. This phenomena is also observed in the RABBIT method [21] which can for example be used to characterize APT, attosecond pulse trains and the measure of the photoemission delay.

4.2 Resolution and Calibration of the spectrometer

As mentioned in earlier sections, the resolution of the CIEL spectrometer has been studied before and after the new configuration. This allows us to insure that the spectrometer performance was unchanged and to know under which conditions we can conduct experiments in the future. Once the magnetic field alignment is controlled and the main coils are set to a value which confines the photoelectron kinetic energies up to 12 eV, ATI photoelectron spectra can be recorded and used to calculate the experimental energy resolution.
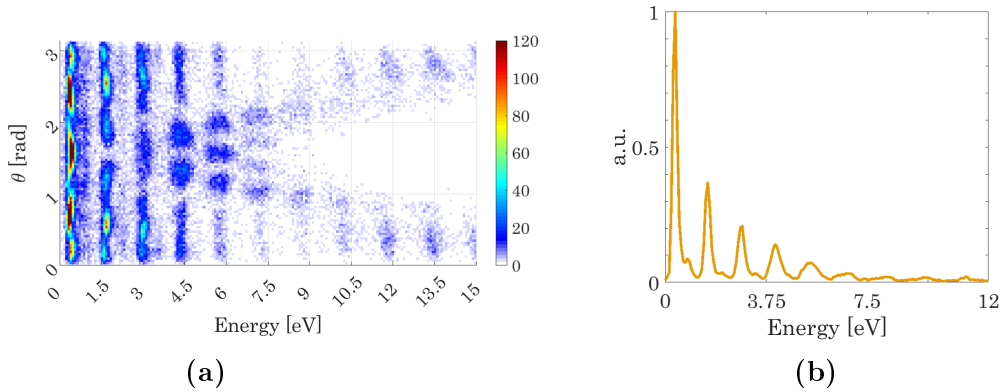

(a)   (b)

Figure 4.2.1: (a) Illustration of ATI kinetic energy distribution integrated along the azimuthal angle and plotted as a function of polar angle. (b) ATI photoelectron energy signal from (a) integrated along the entire polar angle. The energy lines are separated by one photon energy roughly equal to 1.2 eV at 1030 nm.

Figure 4.2.1(a) above shows the kinetic photoelectron energy as a function of the three dimensional polar angle where $\theta = \pi/2$ corresponds to the transverse x-y-plane. The energy peaks are seperated by one photon energy $h\nu$ which is approximately equal to 1.45 eV. The experimental value for the relative resolution $\Delta E_k/E_k$ is obtained by first integrating the energy along the total range of the polar angle. As a result, a one dimensional energy histogram is obtained which is shown in figure 4.2.1(b). After fitting a Gaussian function to every energy peak, the full width at half maximum (FWHM) of each fit can be extracted and used to represent the absolute resolution ΔE_k.

In a first experiment, the resolution is measured in the former horizontal configuration of the spectrometer under different field parameters. For instance, the extraction field is set to both 11 V/cm and 5.5 V/cm with the main magnetic coils set to 8.64 G and 5.9 G respectively. In both cases, magnetic nodes can be avoided.
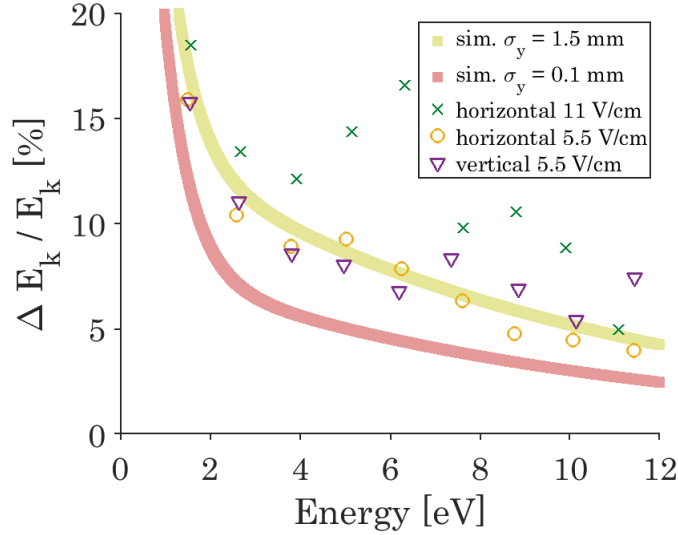
Figure 4.2.2: Energy resolution plotted as a function of energy, experimentally measured in horizontal configuration at 11 V/cm (green crosses) and at 5.5 V/cm (orange circles) and in vertical alignment at 5.5 V/cm (purple triangles). The yellow line shows the simulated energy resolution at an interaction volume equal to $\sigma_x = 0.1$ mm and $\sigma_y = 1.5$ mm while the pink curve corresponds to an interaction volume of $\sigma_x = 0.1$ mm.

Figure 4.2.2 shows the relative energy resolution in percentage as a function of kinetic energy peak values. While the green crosses and the orange circles represent data taken in the horizontal configuration of the spectrometer at an electric field of 5.5 V/cm and 11 V/cm respectively, the purple triangles show the resolution value in the vertical configuration at an electric field equal to 5.5 V/cm. In all experimental measurements, the interaction region is filtered to a spread of 0.1 mm in x-direction and 1.5 mm in y-direction. Moreover, the average theoretical resolution is simulated in two cases (yellow and pink), calculated from equation 3.9 with experimental raw data and calibrated fields. The simulated value shown in the figure 4.2.2 is a mean value determined from the resolution distribution along the polar angle. First, the yellow curve represents the simulated case fitted to the experimental results at 5.5 V/cm with a temporal resolution of $\sigma_t = 0.2$ ns, and a spatial resolution of $\sigma_y = 1.5$ mm and $\sigma_x = 0.1$ mm. Secondly, the pink curve shows the simulated resolution under the ideal temporal response of the detector at $\sigma_t = 0.2$ ns and the spatial resolution of $\sigma_x = \sigma_y = 0.1$mm. In both cases, the ATI linewidth ΔE_{ATI} is set to 180 mV based on [25]. In general, for all cases, the absolute resolution ΔE_k deteriorates with higher energies, thus increases in value. This is due to the fact that the DLD has a limited time resolution of 200 ps and therefore less resolvability at higher TOFs. However, as the increase in ΔE_k is slower than the increase in E_k, the relative resolution $\Delta E_k/E_k$ decreases.

From figure 4.2.2, we can evaluate that a lower extraction field is beneficial to resolve the kinetic energy, since the electrons feel less force from the electrodes and thus travel

slower onto the DLD. Therefore, in a second experiment at the vertical configuration of the spectrometer, an electric field of 5.5 V/cm is chosen with a magnetic field of 5.9 G. A major result from figure 4.2.2 above is that the resolution at vertical configuration remains almost unchanged compared to the horizontal case until an energy of around 7 eV. The relative resolution value evolves from close to 20 % at 1 eV to $5 - 7\%$ at 8 eV. Beyond 7 eV, we observe that the linewidth of the ATI pattern increases in the vertical case and the resolution deteriorates. We believe that this might either be caused by a slight offset in the data calibration. However, the points remain close to the simulated curve in yellow and only differ by 1-3 %. In addition, in the vertical configuration, we increased the pulse energy from 200 μ J to 340 μJ in order to achieve ATI signals along the same energy range. We believe that this might be caused by a change in the laser settings. Since there is almost no change in resolution between the vertical and horizontal alignment of the spectrometer, we can conclude that the magnetic field alignment was not the limiting factor of the resolution.

However, we observe that the interaction volume is a factor that leads to a loss of resolution in the experiment. In the ideal case of the interaction region being equal to a point source, the resolution is only limited by the spatial resolution of the detector such that $\sigma_x = \sigma_y = 0.1$ mm. At this size of the interaction region, the pink curve is simulated and shows a clear improvement in resolution with respect to the yellow curve. However, due to the fact that we use an effusive gas jet in the experiment, the atoms are ionized with an elongation along the laser focus in y-direction. The spread of the signal in x-direction is mainly determined by the thermal distribution of the gas jet. To improve the resolution, the experimental data can be filtered by using the ion signal.
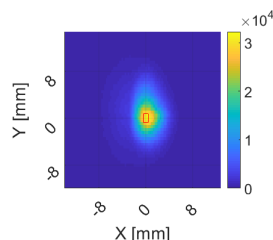

Figure 4.2.3: Two dimensional position signal of the Ions plotted with a filtering window of size 0.8x1.5 mm^2 shown by a red box.

Figure 4.2.3 (a) shows the principle behind the filtering of the data by using the position of the ions. We can clearly see the improvement of the resolution in figure 4.2.2 when the data is narrowed down to a smaller interaction volume. However, when filtering the ion data with a window of 0.1x0.1mm^2, only approximately 100 data points are left which is an insufficient amount for a Gaussian function to be fitted onto. In the future, to obtain a lower interaction volume, both a molecular beam and a tighter focusing could be a solution. If a collimated molecular beam of around 0.5mm is used, the source volume could be improved by a factor of 2-3. However, since we are looking at a multiphoton process for the resolution

experiment, a tight focusing would be most beneficial. This would require a shorter focal length and therefore the placement of a lens inside the vacuum chamber which then limits us in alignment since the chamber is pumped down to ultra-high vacuum.

For lower energies, the energy resolution is mainly limited by the intrinsic linewidth of the ATI experiment ΔE_{ATI} while at higher energies, it is mainly the experimental aspects such as the source volume of the interaction and the temporal response of the detector that limit the resolution.

Chapter 5

Summary and Outlook

In this thesis, we report on the first photoionization experiment of Helium in a dressed field with a new high repetition rate attosecond light source driven by state-of-the-art OPCPA laser technology. Angular resolved photoelectron spectra were measured with the CIEL 3D momentum imaging spectrometer and a plug-in for the calibration and the conversion of the data was developed. We observed that the photoelectron energy spectrum depends on the attosecond pulse trains temporal properties which was controlled by the carrier-to-envelope phase of the driving laser. In the case when two attosecond pulses are generated, the interferences between two consecutive electron-wave-packets can be interpreted in time, where the photoelectron spectrum represents the signal of the slits in the far-field. The infrared phase acts as a phase plate on one of the slits and therefore changes the interference pattern. For three attosecond pulses, both the interference between adjacent generated electron-wave-packets (intracycle) and the interference (intercycle) between the first and the third EWP contributes to the spectrum. The intercycle interference can be understood as the diplacement of the slits in the time domain related to the variation of the temporal phases of the XUV pulses and which is enhanced at shorter infrared pulse durations.

During this work, the coincidence spectrometer CIEL has been changed to facilitate the magnetic field alignment. In both the former and the new configuration, the resolution is studied and concluded to be nearly unchanged and we showed that mainly the source volume that limits the energy resolution.

Within the field of attosecond science, the group in Lund is the first capable to combine state-of-the-art laser technology with pulses at sub-7 fs pulse duration, at 200 kHz repetition rate with a 3D momentum imaging spectrometer. The future experiments can be foreseen:

- Study the behavior of the outgoing electron-wave-packets by performing experiments on different rare gas atoms while changing the CEP. This would require further development wo of the SFA model that was implemented.

- Perform a scan of the delay between the IR and the XUV pulses with our new OPCPA laser system which should allow us to extract the atomic phase, thus the time delay.

Since our SFA model does not yet include the atomic phase, a more sophisticated theory is required.

- Investigation, for instance, in more complex systems such as in molecules or by looking at two electron-wave-packets.

On the experimental side, the energy resolution of the spectrometer could benefit from an upgrade of the effusive gas jet to a molecular beam. This would provide a well-collimated interaction region. Finally, the combination of a new detection technique together with recently developed laser technology may extend the applications of attosecond science in completely new regime where the transition from a rather classical behavior of the electron-wave-packet to quantum mechanical photon transitions can be tested.

Acknowledgements

I would acknowledge all the main people that have helped me to achieve this thesis work.

First of all, my supervisor Mathieu Gisselbrecht, who provided me with a lot of useful tools, his good intuition for physics, his philosophical thoughts and his advanced knowledge for structuring written scientific work. Thank you for your time!

Throughout my thesis, I have been closely working with the MHZ attosecond group. I would like to say a special thank you to Yu-Chen who has been an excellent co-supervisor through his detailed knowledge about his own CIEL spectrometer design, his availability to answer all kinds of questions and his great help in the labs. I am also very thankful to have worked with Sara and Jan Vogelsang who are both very ambitious and excellent researchers and who have helped me to gain a better understanding about the HHG process, about interpreting the photoionization results (mostly Sara) and about how to properly bake a spectrometer and deal with vacuum (mostly Jan). I feel proud to have worked with all three of you!

Moreover, I have had the pleasure to sit in a great office with also Fabian and Ivan. Thanks for your jokes and talks!

The whole attosecond groups combined deserve my thank you for being such a kind, funny and smart bunch of people! Thank you Anne l'Huillier for transmitting your fascination for Physics and for always having an open door, and thank you to the whole division of atomic physics for creating a nice working atmosphere (and lots of opportunities to get free food as a Master student).

I would like to thank my family who has given me the freedom and resources to choose the education path that I wanted and who always supports me with wisdom and love. And thank you Truls for being the funny, understanding and laid-back person you are!

Bibliography

[1] P. Agostini, F. Fabre, G. Mainfray, G. Petite, and N. K. Rahman. Free-Free Transitions Following Six-Photon Ionization of Xenon Atoms. *Phys. Rev. Lett.*, 42:1127, 1979.

[2] F. Amiranoff, S. Baton, D. Bernard, B. Cros, D. Descamps, F. Dorchies, F. Jacquet, V. Malka, J. R. Marquès, G. Matthieussent, P. Miné, A. Modena, P. Mora, J. Morillo, and Z. Najmudin. Observation of laser wakefield acceleration of electrons. *Physical Review Letters*, 81(5):995–998, aug 1998.

[3] S. A. Aseyev, Y. Ni, L. J. Frasinski, H. G. Muller, and M. J. J. Vrakking. Attosecond Angle-Resolved Photoelectron Spectroscopy. *Phys. Rev. Lett.*, 91:223902, 2003.

[4] Benjamin Bolling. Bart Oostenrijk. Anaconda: Analysis of coincidence data, 2018.

[5] Stefanos Carlstroem, Johan Mauritsson, Kenneth J Schafer, Anne L'Huillier, and Mathieu Gisselbrecht. Quantum coherence in photo-ionisation with tailored XUV pulses. *Journal of Physics B: Atomic, Molecular and Optical Physics*, 51(1):015201, nov 2017.

[6] National centers for environmental information. Magnetic field calculators, 2019.

[7] Yu-Chen Cheng. *Ultrafast Photoionization Dynamics Studied with Coincidence Momentum Imaging Spectrometers*. PhD thesis, 2019.

[8] P.B. Corkum. Plasma perspective on strong-field multiphoton ionization. *Phys. Rev. Lett.*, **71**:1994, 1993.

[9] Marcus Dahlstroem. Light-matter interaction on the attosecond timescale, 2011.

[10] J Marcus Dahlström, Diego Guénot, Kathrin Klünder, Matthieu Gisselbrecht, Johan Mauritsson, Anne L'Huillier, Alfred Maquet, and Richard Taïeb. Theory of attosecond delays in laser-assisted photoionization. *Chem. Phys.*, 414:53–64, 2013.

[11] JM Dahlström, Anne L'Huillier, and A Maquet. Introduction to attosecond delays in photoionization. *Journal of Physics B: Atomic, Molecular and Optical Physics*, 45(18):183001, aug 2012.

[12] R. Dorner, V. Mergel, O. Jagutzki, L. Spielberger, J. Ullrich, R. Moshammer, and
H. Schmidt-Bocking. Cold Target Recoil Ion Momentum Spectroscopy: a 'momentum
microscope' to view atomic collision dynamics. *Physics Reports*, 330:95–192, 2000.

[13] P. Eckle, A. N. Pfeiffer, C. Cirelli, A. Staudte, R. Dorner, H. G. Muller, M. Buttiker,
and U. Keller. Attosecond ionization and tunneling delay time measurements in he-
lium. *Science*, 322(5907):1525–1529, dec 2008.

[14] J. Gagnon and V.S. Yakovlev. The direct evaluation of attosecond chirp from a
streaking measurement. *Applied Physics B*, 103:303–309, 2011.

[15] M. Gisselbrecht, A. Huetz, M. Lavollee, T. J. Reddish, and D. P. Seccombe. Opti-
mization of momentum imaging systems using electric and magnetic fields. *Review of
Scientific Instruments*, 76(1):013105, 2005.

[16] D. Guénot, E. Balogh D. Kroon, E. W. Larsen, M. Kotur, M. Miranda, T. Fordell,
P. Johnsson, J. Mauritsson, C. L. Arnold M. Gisselbrechtand K. Varjú, T. Carette,
A. S. Kheifets, E. Lindroth, A. L'Huillier, and J. M. Dahlström. Measurements of
relative photoemission time delays in noble gas atoms. *(submitted)*.

[17] Chen Guo, Anne Harth, Stefanos Carlström, Yu-Chen Cheng, Sara Mikaelsson, Erik
Mårsell, Christoph Heyl, Miguel Miranda, Mathieu Gisselbrecht, Mette B Gaarde,
Kenneth J Schafer, Anders Mikkelsen, Johan Mauritsson, Cord L Arnold, and Anne
L'Huillier. Phase control of attosecond pulses in a train. *J. Phys. B: At., Mol. Opt.
Phys.*, 51(3):034006, jan 2018.

[18] Anne Harth, Chen Guo, Yu-Chen Cheng, Arthur Losquin, Miguel Miranda, Sara
Mikaelsson, Christoph Michael Heyl, Oliver Prochnow, Jan Ahrens, Uwe Morgner,
Anne L'Huillier, and Cord L Arnold. Compact 200 kHz HHG source driven by a
few-cycle OPCPA. *J. Opt.*, 20(1):014007, dec 2017.

[19] Wolfram Research Inc. Spherical coordinates, 2019.

[20] M. Isinger, D. Busto, S. Mikaelsson, S. Zhong, C. Guo, P. Salieres, C. L. Arnold,
A. LHuillier, and M. Gisselbrecht. Accuracy and precision of the RABBIT technique.
*Philosophical Transactions of the Royal Society A: Mathematical, Physical and Engi-
neering Sciences*, 377(2145):20170475, may 2019.

[21] M. Isinger, R. J. Squibb, D. Busto, S. Zhong, A. Harth, D. Kroon, S. Nandi, C. L.
Arnold, M. Miranda, J. M. Dahlstroem, E. Lindroth, R. Feifel, M. Gisselbrecht,
and A. L'Huillier. Photoionization in the time and frequency domain. *Science*,
358(6365):893–896, nov 2017.

[22] J. D. Jackson. *Classical electrodynamics*. Cloth. Wiley, 1999.

[23] Álvaro Jiménez-Galán, Fernando Martín, and Luca Argenti. Two-photon finite-pulse model for resonant transitions in attosecond experiments. *Physical Review A*, 93(2), feb 2016.

[24] Per Johnsson. *Attosecond optical and electronic wave packets*. PhD thesis, 2006.

[25] N G Kling, D Paul, A Gura, G Laurent, S De, H Li, Z Wang, B Ahn, C H Kim, T K Kim, I V Litvinyuk, C L Cocke, I Ben-Itzhak, D Kim, and M F Kling. Thick-lens velocity-map imaging spectrometer with high resolution for high-energy charged particles. *Journal of Instrumentation*, 9(05):P05005–P05005, may 2014.

[26] J. L. Krause, K. J. Schafer, and K. C. Kulander. High-order harmonic generation from atoms and ions in the high intensity regime. *Phys. Rev. Lett.*, **68**:3535, 1992.

[27] F. Krausz and M. Ivanov. Attosecond physics. *Rev. Mod. Phys.*, 81(1):163–234, 2009.

[28] Ferenc Krausz and Misha Ivanov. Attosecond physics. *Reviews of Modern Physics*, 81(1):163–234, feb 2009.

[29] William R. Leo. *Techniques for Nuclear and Particle Physics Experiments*. 1994.

[30] M. Lewenstein, Ph. Balcou, M.Yu. Ivanov, A. L'Huillier, and P.B. Corkum. Theory of high-order harmonic generation by low-frequency laser fields. *Phys. Rev. A*, 49:2117, 1994.

[31] A. L'Huillier and Ph. Balcou. High-order harmonic generation in rare gases with an intense short-pulse laser. *Phys. Rev. Lett.*, 70:774, 1993.

[32] E. Lorek, E. W. Larsen, C. M. Heyl, S. Carlstr om, D. Paleček, D. Zigmantas, and J. Mauritsson. High-order harmonic generation using a high-repetition-rate turnkey laser. *Rev. Sci. Instrum.*, 85(12):–, 2014.

[33] Chih-Hsuan Lu, Tobias Witting, Anton Husakou, Marc J.J. Vrakking, A. H. Kung, and Federico J. Furch. Sub-4 fs laser pulses at high average power and high repetition rate from an all-solid-state setup. *Optics Express*, 26(7):8941, mar 2018.

[34] M. Miranda, T. Fordell, C. Arnold, A. L'Huillier, and H. Crespo. Simultaneous compression and characterization of ultrashort laser pulses using chirped mirrors and glass wedges. *Opt. Express*, 20(1):688–697, Jan 2012.

[35] P _ M Paul, ES Toma, P Breger, Genevive Mullot, F Augé, Ph Balcou, HG Muller, and P Agostini. Observation of a train of attosecond pulses from high harmonic generation. *Science*, 292(5522):1689–1692, jun 2001.

[36] T. Pfeifer, L. Gallmann, M. J. Abel, D. M. Neumark, and S. R. Leone. Single attosecond pulse generation in the multicycle-driver regime by adding a weak second-harmonic field. *Opt. Lett.*, 31:975, 2006.

[37] F. Quéré, Y. Mairesse, and J. Itatani. Temporal characterization of attosecond XUV fields. *J. Mod. Opt.*, 52:339, 2005.

[38] Linnea Rading, Jan Lahl, Sylvain Maclot, Filippo Campi, Hélène Coudert-Alteirac, Bart Oostenrijk, Jasper Peschel, Hampus Wikmark, Piotr Rudawski, Mathieu Gisselbrecht, and Per Johnsson. A versatile velocity map ion-electron covariance imaging spectrometer for high-intensity XUV experiments. *Applied Sciences*, 8(6):998, jun 2018.

[39] Piotr Rudawski, Anne Harth, Chen Guo, Eleonora Lorek, Miguel Miranda, ChristophM. Heyl, EsbenW. Larsen, Jan Ahrens, Oliver Prochnow, Thomas Binhammer, Uwe Morgner, Johan Mauritsson, Anne L'Huillier, and Cord L. Arnold. Carrier-envelope phase dependent high-order harmonic generation with a high-repetition rate opcpa-system. *Eur. Phys. J. D*, 69(3):147–152, 2015.

[40] J. J. Sakurai. *Modern Quantum Mechanics*. Addison-Wesley Publishing Co., 1994.

[41] B. E. A. Saleh and M. C. Teich. *Fundamentals of Photonics*. John Wiley and Sons, 2007.

[42] G. Sansone, F. Kelkensberg, J. F. Pérez-Torres, F. Morales, M. F. Kling, W. Siu, O. Ghafur, P. Johnsson, M. Swoboda, E. Benedetti, F. Ferrari, F. Lépine, J. L. Sanz-Vicario, S. Zherebtsov, I. Znakovskaya, A. LHuillier, M. Yu. Ivanov, M. Nisoli, F. Martìn, and M. J. J. Vrakking. Electron localization following attosecond molecular photoionization. *Nature*, 465:763766, 2010.

[43] G. Sansone, L. Poletto, and M. Nisoli. High-energy attosecond light sources. *Nat Photon*, 5(11):655–663, 2011.

[44] D. Strickland and G. Mourou. Compression of amplified chirped optical pulses. *Opt. Commun.*, **56**:219, 1985.

[45] K. Varjú, Y. Mairesse, B. Carre, M. B. Gaarde, P. Johnsson, S. Kazamias, R. Lopez-Martens, J. Mauritsson, K. J. Schafer, Ph. Balcou, A. L'Huillier, and P. Salières. Frequency chirp of harmonic and attosecond pulses. *J. Mod. Opt.*, 52:379, 2005.

[46] C.-G. Wahlström, J. Larsson, A. Persson, T. Starczewski, S. Svanberg, P. Salières, Ph. Balcou, and Anne L'Huillier. High-order harmonic generation in rare gases with an intense short-pulse laser. *Physical Review A*, 48(6):4709–4720, Dec 1993.

[47] Hampus Wikmark, Chen Guo, Jan Vogelsang, Peter W. Smorenburg, Hélène Coudert-Alteirac, Jan Lahl, Jasper Peschel, Piotr Rudawski, Hugo Dacasa, Stefanos Carlström, Sylvain Maclot, Mette B. Gaarde, Per Johnsson, Cord L. Arnold, and Anne L'Huillier. Spatio-temporal coupling of attosecond pulses. *Proceedings of the National Academy of Sciences*, 2019.

[48] Stefan Witte and K. S. E. Eikema. Ultrafast optical parametric chirped-pulse amplification. *IEEE Journal of Selected Topics in Quantum Electronics*, 18(1):296–307, jan 2012.

Appendix A

Momentum Imaging derivation

The electrons that are generated in the coincidence imaging spectrometer are exposed to the Lorentz force due to the applied electric and magnetic field,

$$\mathbf{F}_L = q(\mathbf{E} + \mathbf{v} \times \mathbf{B}) \tag{A.1}$$

where the electric field $\mathbf{E} = \mathrm{E}\ \hat{\mathbf{e}}_z$ and the magnetic field $\mathbf{B} = \mathrm{B}\ \hat{\mathbf{e}}_z$ are oriented along the normal axis central to the spectrometer.

The equations of motion can be classically solved and result in the following time-dependent coordinates [15]:

$$x(t) = \frac{1}{qB}p_y(1 - cos(\omega t)) + \frac{1}{qB}\ p_x sin(\omega t) \tag{A.2}$$

$$y(t) = \frac{1}{qB}p_x(cos(\omega t) - 1) + \frac{1}{qB}p_y sin(\omega t) \tag{A.3}$$

where p_x and p_y represent the initial momenta at the point of interaction and $\omega = \frac{qB}{m}$ is the cyclotron frequency. After the ionization event within the interaction plane of the spectrometer, the electrons travel along a helical trajectory with radius $r = \sqrt{x(t)^2 + y(t)^2}$ with time t. The time that it takes for the electron to reach the detector is called time-of-flight (TOF).

A $4\ \pi$ collection efficiency can be achieved when r is less than the radius of the electron detector. By rearranging the above derived equations and using matrix representation, the initial momenta can be expressed as :

$$\begin{bmatrix} p_x \\ p_y \end{bmatrix} = \frac{qB}{2} \cdot \begin{bmatrix} M(\omega t) & 1 \\ 1 & -M(\omega t) \end{bmatrix} \begin{bmatrix} x \\ y \end{bmatrix} \tag{A.4}$$

where $M(\omega t) = csc(\omega t) + cot(\omega t)$.

Therefore, by determining the two-dimensional position coordinates x and y on the electron detector, the initial momentum of the electron can be revealed in two dimensions. One can conclude that the magnetic field only influences the initial momentum components

p_x and p_y. The initial momentum in third dimension p_z is determined through the difference in initial and final momentum Δp such that

$$\Delta p = p_{z,f} - p_z. \tag{A.5}$$

By classical mechanics, it is known that $\Delta p = F \Delta t$ where F represents the applied force onto the electron, Δp is the change in momentum and Δt is the difference in travel time of the electron which is the TOF of the electron, such that $\Delta t = TOF$. Along the z-axis, a force $F = qE$ given by the electric extraction field E acts onto the electron. The difference in momentum can thus be expressed as

$$\Delta p = qE \cdot TOF. \tag{A.6}$$

The final momentum $p_{z,f}$ is derived by using the total energy acquired by the electron from the interaction to the detector. The total final energy ϵ_f is equal to the sum of the initial energy of the electron at the point of interaction and the energy acquired by the force $F = qE$, which is expressed by

$$\epsilon_f = \frac{p^2}{2m} + qE \cdot d. \tag{A.7}$$

By converting the final energy ϵ_f to momentum $p_{z,f}$, using the equation $\epsilon_f = \frac{p_{z,f}}{2m}$, the change in momentum along the extraction region can thus be written as

$$\Delta p = \sqrt{p_z^2 + 2m \cdot qE \cdot d} - p_z. \tag{A.8}$$

Inserting the expression A.6 into equation A.8 leads to a final expression of the TOF in the first region of the spectrometer, the extraction region, given by

$$TOF_1 = \frac{\sqrt{p_z^2 + 2mqEd} - p_z}{qE}. \tag{A.9}$$

Likewise, the electron TOF can be defined in the drift tube region by using the fact that the electron momentum acquired by passing through this region isequal to $p_{zf} = m\frac{l}{TOF_2}$ where l represents the length of the drift tube and m the electron mass.

$$TOF_2 = \frac{lm}{\sqrt{p_z^2 + 2mqEd}} \tag{A.10}$$

In our case, the energy acquired by passing through the extraction and drift region is two orders of magnitude greater than the initial energy of the electrons ϵ . Therefore, the total TOF can be approximated by using $p_z << \sqrt{qEmd}$ such that the momentum in z-direction can be expressed by:

$$p_z = qE\left(TOF_1 + TOF_2 - t_0\right) \tag{A.11}$$

where t_0 corresponds to the time it takes the electron to reach the detector without initial p_z momentum. It is defined according to [15] by:

$$t_0 = \sqrt{\frac{2md}{qE}}\frac{2d+l}{2d} \tag{A.12}$$

In conclusion, equation 3.2 and 3.3 clearly show that thanks to the magnetic field B parallel to the electric field, a helix is formed which leads to a collection efficiency of 4π. Moreover, the equations show that the collected 3D data, x,y and TOF allows for 3D momentum reconstruction, thus for a complete kinematic picture.

Appendix B

Spectrometer- vertical design

Overall, the CIEL spectrometer is built using a chamber for atomic and molecular physics (CAMP) which is operated under ultrahigh vacuum (UHV) at $10^{-9} - 10^{-10}$ mbar without gas at $10^{-6} - 10^{-7}$ mbar with gas. The spectrometer is a separate part of the CIEL and is embedded into the CAMP chamber. It incorporates a drift tube, an extraction region, as well as an aluminium structure holding the chamber together. As part of this thesis work, the CIEL spectrometer is rebuilt in a vertical alignment. The total work including design, building and testing phases took roughly 6 months.
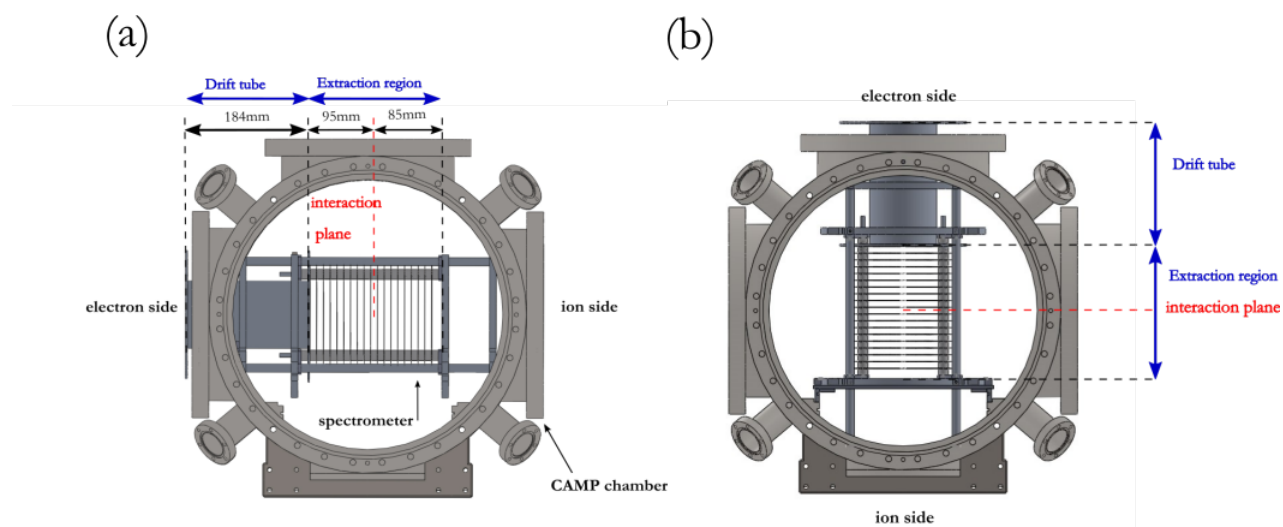
Inside frame

Figure B.0.1: (a) Horizontal design of the spectrometer held by the CAMP chamber directly, (b) Vertical design of the spectrometer with newly designed frame connected to the CAMP chamber.

In the horizontal alignment shown in figure B.0.1, the spectrometer is held by pre-designed feet in the CAMP chamber. It can easily be de- and attached by sliding it out of the CAMP chamber. However, for the vertical alignment, a new frame needs to be designed that hold the spectrometer while placeing the interaction plane in the middle of the CAMP chamber. Hereby, the design needs to restrict the spectrometers movement in all three dimensions to ensure its stability during an experiment. For the design, one needs to remember that, compared to a CAD drawing, the built frame in reality might have a slight offset in dimensions. Thus, it needs to be designed in CAD with a margin for screw holes and distances.
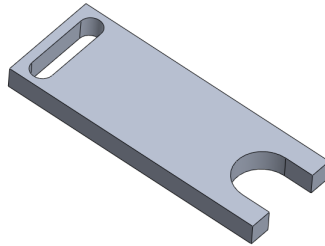

Figure B.0.2: Clamp as part of the frame holding the spectrometer vertically. The screw hole is elongated to ensure variable placement.

In our case, larger screwholes also serve as an alignment purpose to position the frame. Four clamps restrict the spectrometer in transverse direction. In order to restrict the movement along the spectrometer axis, two feet are placed underneath the spectrometer and a washer is screwed to these feet so that half of it lies on top of the spectrometers aluminum frame and blocks its movement upwards. To facilitate the pumping of the CAMP chamber to UHV, it is avoided to have large areas of plane surface connections.

The detectors are now installed on the top and bottom side, and the pump and the gas insertion needle are installed on the side. Special attention needs to be paid to the pump as it is sensitive to movements of the chamber which could be caused by a force due to screw tightening or released pressure differences.
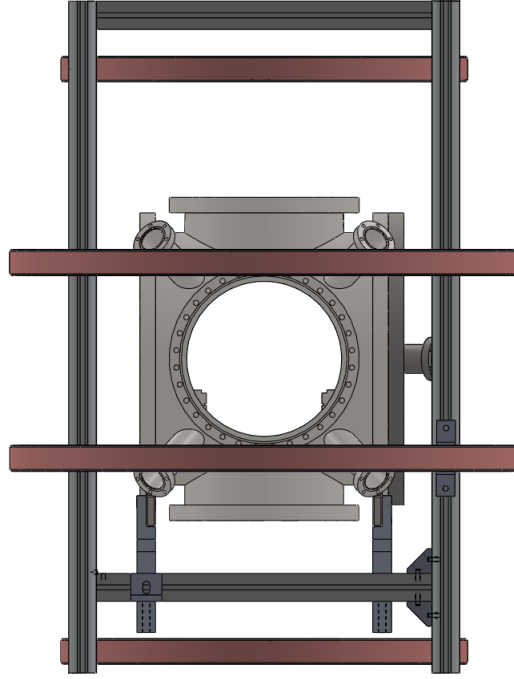
Outside frame

Figure B.0.3: Camp chamber without spectrometer inside and outer frame holding the four magnetic coils at an equal distance. The coils are hold with l-shaped clamps that are connected to the minitec frame.

Changing the alignment of the spectrometer requires a reorientation of the magnetic coils along the spectrometer axis. When building an outer frame to hold the coils, we choose a minitec structure. A non-magnetic material needs to be chosen for screws and other parts to minimize the influence on the magnetic environment. As before, the four coils are installed at an even distance between each other. The compact outer frame allows for installation of compensating coils to cancel out the contribution of the transverse magnetic field components. The field of the magnetic coils can be simulated with SIMION .

The main coils are calibrated as presented in the main thesis text. However, in order to compensate the magnetic field, the compensating coils need to be calibrated. For that purpose, the magnetic field created by two pairs of coils is first simulated using the Biot-Savart law [22]:

$$d\mathbf{B} = N\,I\,\frac{\mu_0}{4\pi}\frac{d\mathbf{l}\times\mathbf{x}}{|\mathbf{x}|^3}. \tag{B.1}$$

This helps us to determine the spacing between the coil pairs. Afterwards, we apply a current to the compensating coils and vary the current applied to the main coils. Once the

position of the electron signal does not vary with the current applied to the main coils, the compensating coils are set to the right value.

There are two main advantages with a vertical alignment of the spectrometer. First, the earth magnetic field in the laboratory frame in Sweden exerts a more important vertical than horizontal component. The vertical alignment therefore facilitates the transverse magnetic field compensation and the overall alignment. Moreover, there is more room to install a molecular beam on the side of the CAMP chamber for future experiments, since space is limited in height and the molecular beam could barely be reachable.